Journal of Sound and Vibration 573 (2024) 118196

Contents lists available at ScienceDirect

Journal of Sound and Vibration

journal homepage: www.elsevier.com/locate/jsvi

# Dynamical analysis and design theory for active bistable vibration isolators considering delay effect

Yifan Liu [a], Bo Yan [b], Li Cheng [a,*]

[a] Department of Mechanical Engineering, The Hong Kong Polytechnic University, Kowloon, Hong Kong, China
[b] School of Mechanical Engineering, Zhejiang Sci-Tech University, Hangzhou, 310018, China

ARTICLE INFO

*Keywords:*
Active bistable vibration isolator
Delayed PD control
HSLDS characteristics
Delay-coupled bistable dynamics
Ultra-low-frequency vibration isolation

ABSTRACT

Bistable vibration isolators (BVIs), which can undergo intra- and inter-well motions, have recently gained much attention as different motions can lead to different low-frequency isolation properties. To fully exploit the strength of BVIs, feedback actuation is injected into a classic three-spring-two-link bistable structure, and the classic PD control is applied to tune system's stiffness and damping. Moreover, the effect of the inevitable loop delay on BVI performance is considered. Operable regions of control parameters to maintain bistable characteristics and robustness regions where active BVIs are operable regardless of delay perturbations are determined. Besides, bistable dynamics, complicated by the transcendentality caused by delay, are investigated. By taking the BVI as phase zero, the number of variables to be solved is reduced, and an efficient frequency-sweeping-based calculation procedure is proposed. The BVI is evaluated by force and displacement transmissibility, showing that both intra- and inter-well motions benefit vibration isolation. For the former, the BVI yields broadband vibration isolation similar to conventional high-static-low-dynamics-stiffness vibration isolators. For the latter, an isolation valley can occur, resulting in exclusive ultra-low-frequency vibration isolation. Furthermore, properly tuning feedback actuation enhances the vibration isolation performance in both cases, and the often-overlooked loop delay can play a very positive role. Finally, the mechanism of isolation valley is qualitatively elucidated. The presented theories, including control stability analysis, delay-coupled nonlinear dynamical analysis, and beneficial parameter tuning, establish a basic design framework for active BVIs.

## 1. Introduction

The importance of vibration reduction cannot be over-emphasized. We consider vibration isolation techniques to reduce the vibration transmission for structural protection. Early vibration isolators are typically linear structures [1–3], which take effect only when the vibration frequency is greater than $\sqrt{2}$ times the natural frequency of the vibration isolator itself [4,5]. Clearly, the trade-off between a wider isolation frequency band and a stronger support capacity limits the applications of linear vibration isolators [6]. For this, research interests rise in nonlinear vibration isolators with high-static-low-dynamic-stiffness (HSLDS) characteristics, which achieve broadband vibration isolation without reducing the static supporting capacity [6–8].

The quasi-zero-stiffness (QZS) isolator is one extensively studied type of HSLDS isolators [9], and the classic three-spring

* Corresponding author.
*E-mail address:* li.cheng@polyu.edu.hk (L. Cheng).

https://doi.org/10.1016/j.jsv.2023.118196
Received 20 August 2023; Received in revised form 20 November 2023; Accepted 30 November 2023
Available online 6 December 2023

configuration proposed in [6] is widely considered. Kovacic et al. [10] found that the nonlinearity and pre-compression of two oblique springs improved the static QZS mechanism. Carrella et al. [11,12] demonstrated the superiority of HSLDS vibration isolators over linear ones by evaluating the force and displacement transmissibility. Brennan et al. [13] determined the jump frequency of frequency responses and the force excitation threshold for which jumping behaviors can occur. Later, various QZS or HSLDS structures were proposed. The construction of HSLDS structures using springs and magnets can be found in [7,14]. Zhou et al. [15] achieved QZS characteristics using cam–roller–spring mechanisms and obtained a piecewise nonlinear isolator with a low isolation frequency of 3 Hz. Ye et al. [16] designed a coupled translational-rotational QZS system to isolate both translational and rotational vibrations. Besides, X-shaped structures were found to exhibit QZS characteristics over a broader displacement region without reducing the load capacity [17–19]. Yan et al. [20] introduced the QZS construction using nonlinear structures. Wang et al. [21] investigated the stiffness effect on vibration isolation and the associated design rules. In addition, the beneficial design of active HSLDS vibration isolators by manipulating the delay in the feedback loop can be referred to [22–26], where properly delayed vibration isolators exhibited expedited response speed and extended isolation bands.

Unlike QZS or HSLDS isolators that have only one equilibrium, bistable structures exhibit two equilibria, and the bistable dynamics can be trapped either in one of the equilibria or between the two. Benefiting from the large amplitude of the inter-well motions in the latter case, bistable structures are widely used for energy harvesting [27–29]. On the other hand, bistable structures have also been used for vibration isolation over the last decade, thus creating the concept of bistable vibration isolators (BVIs). For instance, Johnson et al. [30] achieved a high damping effect using inter-well motions to increase power dissipation. Lu et al. [31] constructed a two-stage vibration isolator with composite plates and improved the isolation performance using bistable properties. Ishida et al. [32] reported a bistable foldable structure-based isolator and suppressed the resonance frequency to 0.24 Hz. Yang et al. [33] designed an innovative bistable electromagnetic actuator using elastic boundary and reduced vibration by more than 90 % via integrating feedback control. Moreover, the benefits of BVIs over linear isolators were demonstrated by a dual-stage case in [34], where a valley frequency response was also observed to enhance vibration isolation. Thereafter, Yan et al. [35] designed a BVI by injecting permanent magnets into a linear mass-spring-damper system and observed that the valley frequency response induced by inter-well motions achieved ultra-low-frequency vibration isolation. The experimental setup in [35] was then modified in [36], where the newly introduced nonlinear electromagnetic shunt damping further enhanced isolation. Subsequently, a design theory of passive BVIs was summarized in [37]. Besides, Noh et al. [38] showed that a BVI can offer a broader isolation band and lower resonance compared with conventional HSLDS vibration isolators.

While various passive and active BVIs have been proposed and analyzed, we believe that how to fully utilize the advantages of this relatively new concept has not been fully explored. For instance, the active BVI in [33] focuses more on intra-well motions. The passive BVI in [38] is mainly used to isolate force excitations. Indeed, the ultra-low-frequency vibration isolation achieved by the valley response when undergoing inter-well motions found in our previous works [35–37] are exclusive, while the valley width is narrow, and how it can be manipulated to be practically used has not been enough discussion. Hence, we introduce an additional feedback actuation to tune the isolator dynamics in real-time, aiming to fully exploit the strength of BVIs whether operating with intra- or inter-well motions or handling force or motion excitations. On the other hand, delay is inevitable in real control loops with notable effects widely observed to benefit HSLDS isolators [22–26], vibration absorbers [39–44], and some multi-stable systems [45]. Thus, the possible beneficial roles that the delay can play in an active BVI system also deserves to be investigated. Given that asymmetric dynamics would lead to unilateral wear and that shallower potential wells benefit the switch between inter- and intra-well operating modes, the analysis is based on a classic symmetric three-spring-two-link construction to focus on properly designing and tuning the feedback actuation. Without loss of generality, a delayed PD control is adopted to tune the stiffness and damping while considering the delay effect, yielding our threefold main contributions as follows.

First, feedback actuation design criteria for bistable characteristics and robust control stability are proposed, and the inherent loop delay is taken as an additional tunable control parameter to seek performance enhancement. Second, the resulting delay-coupled bistable dynamics are established by generalizing our recent work [46], yielding a frequency-sweeping procedure for efficient dynamical analysis. Third, the tuning mechanism of feedback actuation to enhance the BVI performance is investigated. The extended isolation valley and the operable valley positions indicate that active BVIs provide a practical solution to isolate ultra-low-frequency vibrations. Particularly, the mechanism of isolation valley is qualitatively elucidated. In this sense, the unique strength of BVIs over the conventional HSLDS vibration isolators can be clearly established.

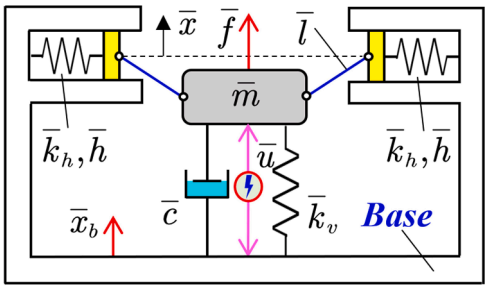


**Fig. 1.** Schematic model of a bistable structure with three springs and two links.

In what follows, Section 2 establishes bistable characteristics. Section 3 introduces the design rules of feedback actuation and determines the operable regions of control parameters for stability and control robustness. Section 4 handles the bistable dynamics. Section 5 evaluates the BVI performance by force and displacement transmissibility, analyzes the parametric effects on vibration isolation, and qualitatively investigates the isolation valley for ultra-low-frequency vibration isolation. Section 6 draws conclusions. Italic symbols without a bar superscript '$\overline{\square}$' stand for dimensionless quantities.

## 2. Mathematical model

The considered BVI construction shown in Fig. 1 was initially designed as a QZS vibration isolator [21,22]. Three linear springs are used: one denoted by $\overline{k}_v$ is placed vertically for suspension, and the other two by $\overline{k}_h$ lie horizontally to create negative stiffness in the vertical direction. The proof mass $\overline{m}$ is connected to the two horizontal springs $\overline{k}_h$ with two links $\overline{l}$, while the connection to the vertical spring $\overline{k}_v$ is rigid. Clearly, the two horizontal springs must be compressed to activate the bistable characteristics, and the compression is $\overline{h}$. In addition, $\overline{f}$ and $\overline{x}_b$ are the force and base excitations, respectively. The linear viscous damper is denoted by $\overline{c}$, and $\overline{u}$ represents the feedback actuation to be designed.

### 2.1. Bistable characteristics

The parametric conditions for the bistable characteristics of the construction in Fig. 1 have been established in our previous work [46] based on potential energy analysis, and we here adopt an alternative procedure using restoring force for simplification. Let us first exclude the feedback actuation $\overline{u}$ and the two external excitations $\overline{f}$ and $\overline{x}_b$. The dynamics are then governed by

$$\overline{m}\ddot{\overline{x}} + \overline{c}\dot{\overline{x}} + \overline{F}(\overline{x}) = 0, \tag{1}$$

where the displacement $\overline{x}$ is a function of the physical time $\overline{t}$, and $\overline{F}$ is the restoring force of the springs satisfying

$$\overline{F}(\overline{x}) = \overline{k}_v\overline{x} - 2\overline{k}_h\left[\overline{h} - \left(\overline{l} - \sqrt{\overline{l}^2 - \overline{x}^2}\right)\right]\frac{\overline{x}}{\sqrt{\overline{l}^2 - \overline{x}^2}}. \tag{2}$$

Introducing the following parameters

$$\overline{\omega}_n = \sqrt{\frac{\overline{k}_v}{\overline{m}}}, \zeta = \frac{\overline{c}}{2\overline{m}\overline{\omega}_n}, t = \overline{t}\overline{\omega}_n, F = \frac{\overline{F}}{\overline{k}_v\overline{l}}, k = \frac{\overline{k}_h}{\overline{k}_v}, x = \frac{\overline{x}}{\overline{l}}, h = \frac{\overline{h}}{\overline{l}}, \tag{3}$$

where $|x| < 1$ due to the mechanical constraint $|\overline{x}| < \overline{l}$, into (1) leads to dimensionless governing equation

$$\ddot{x} + 2\zeta\dot{x} + F(x) = 0, \tag{4}$$

in which the dimensionless total restoring force is

$$F(x) = x - 2k\left(h - 1 + \sqrt{1 - x^2}\right)\frac{x}{\sqrt{1 - x^2}}. \tag{5}$$

The bistable characteristics mean that the proof mass is unstable at $x = 0$, leading to negative stiffness at this point

$$K(x) = \frac{\partial F(x)}{\partial x} = 1 - 2k\left(1 - \frac{1 - h}{(1 - x^2)^{3/2}}\right) \mapsto K(x=0) = 1 - 2kh < 0. \tag{6}$$

Once the bistable proof mass at $x = 0$ encounters a small perturbation, it leaves from this point to two new stable equilibria symmetric about $x = 0$. Besides, the total restoring force should be balanced at such two stable equilibria leading to $F(x) = 0$, which has a fixed solution $x_0 = 0$ corresponding to the unstable saddle equilibrium, and the other two for the stable ones labeled as

$$x_{1,2} = \mp\sqrt{\frac{-4k^2h^2 + 8k^2h - 4k + 1}{(2k - 1)^2}} \tag{7}$$

exist only if the condition (6) holds. Note that the two equilibria $x_{1,2}$ make sense only if $|x_{1,2}| < 1$ so that $h < 1$ as per (7). Combining with (6), we can obtain the parametric condition for bistable characteristics as

$$\left[h \in \left(\frac{1}{2k}, 1\right), k > \frac{1}{2}\right] or \left[k > \frac{1}{2h}, h < 1\right]. \tag{8}$$

Furthermore, the stable and unstable equilibria correspond to the potential well and peak, respectively, and the potential energy stored in the three springs can be derived from (5) as

$$E(x) = \frac{1}{2}x^2 + k\left[h - \left(1 - \sqrt{1 - x^2}\right)\right]^2. \tag{9}$$

With the bistable condition (8), the energy barrier is defined as

$$E_b = E(x = x_0) - E\big(x = x_{1,2}\big) = \frac{(2hk-1)^2}{4k-2}. \tag{10}$$

### 2.2. Potential well

The smaller the energy barrier $E_b$ is, the easier for the proof mass to cross the energy peak $x_0$ and then oscillate between the two stable equilibrium points $x_1$ and $x_2$ once excited. Selecting $h = 0.4$ yields the bistable condition $k > 1.25$ in light of (8), and the associated variations of the potential energy $E$ concerning the $k$ values are depicted in Fig. 2(a).

From Fig. 2(a), potential wells appear when $k > 1.25$ agreeing with (8), and the red curve denoting the positions of the two stable equilibrium points $x_1$ and $x_2$ always crosses such wells. Besides, increasing $k$ deepens the potential wells and separates the two stable equilibrium points. More specifically, Fig. 2(b) and Fig. 2(c) depict the variations of the energy barrier $E_b$ and the equilibrium positions with respect to the parametric pair $(h, k)$, respectively, showing that an increase in either $k$ or $h$ raises $E_b$ and enlarges the distance between the two stable equilibrium points. Hence, we can tune $(h, k)$ to activate bistable characteristics by tactically manipulating the energy barrier $E_b$.

### 2.3. Phase portrait

Phase portrait depicts the transient process of bistable dynamics. Selecting $h = 0.4$, the phase portraits governed by Eqs. (4) and (8) for four pairs of $(\zeta, k)$ are shown in Fig. 3.

The two stable equilibria $x_1$ and $x_2$ governed by (7) and the unstable one $x_0 = 0$ can be more clearly observed in Fig. 3. Comparing the left two subplots Fig. 3(a) and (b)) with the right two shows that raising the energy barrier $E_b$ by increasing $k$ makes it more difficult for the proof mass to escape from the stable equilibrium point. On the other hand, comparing the upper two subplots with the lower two reveals that increasing the damping $\zeta$ would help achieve convergence, although it does not affect equilibrium points as per ((7). Note from Fig. 3(a) that a magenta orbit crosses both $x_1$ and $x_2$, which is the so-called inter-well or snap-through motion and is widely used for energy harvesting owing to the large motion amplitude. Furthermore, one can find that raising the energy barrier $E_b$ and the damping $\zeta$ both suppress the snap-through motions. Also, it is relevant to note that the dynamical orbits with the initial condition at the critical mechanical constraint $|x| = 1$ do not exist since the two links are vertical in this case, leading to a force-dead link configuration.

## 3. Feedback control and system stability

We now inject feedback actuation into the BVI while considering the inevitable loop delay. For bistable characteristics, the feedback actuation should not change system equilibria and their stability. For robustness, the operable parametric ranges where the system stability and bistable characteristics are independent of delay perturbations are determined.

### 3.1. Control logic design

Revisiting Fig. 3, tuning damping $\zeta$ and stiffness $k$ (i.e., the energy barrier $E_b$) both benefit convergence. Since the restoring forces resulting from such two parameters respectively correspond to the displacement $\bar{x}$ and velocity $\dot{\bar{x}}$, we consider the classic PD-type

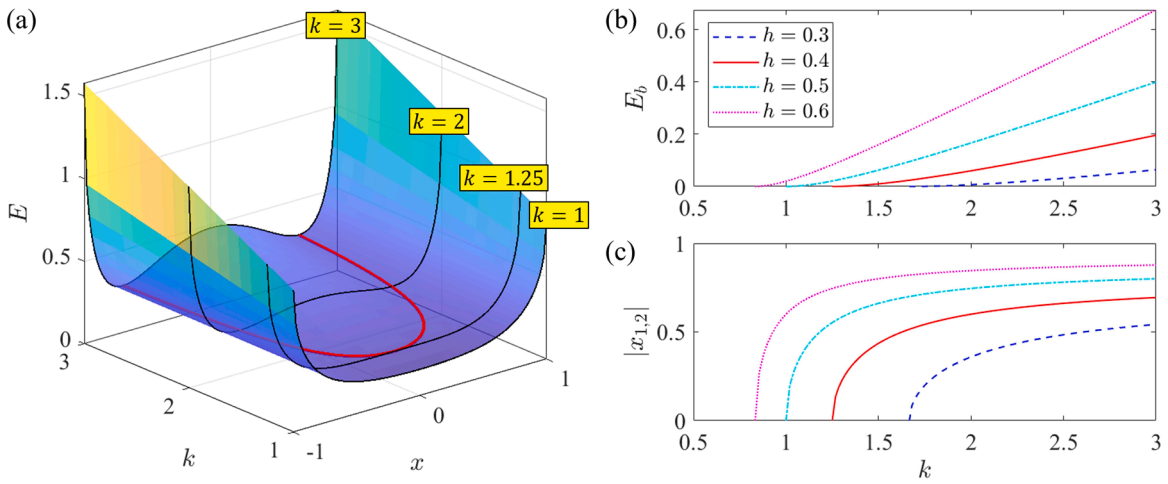


**Fig. 2.** (a). Potential energy $E$ versus $k$ for $h = 0.4$. (b). Potential barrier $E_b$ versus $k$ for four selected $h$ values. (c). Positions of the two stable equilibria versus $k$ for four selected $h$ values.

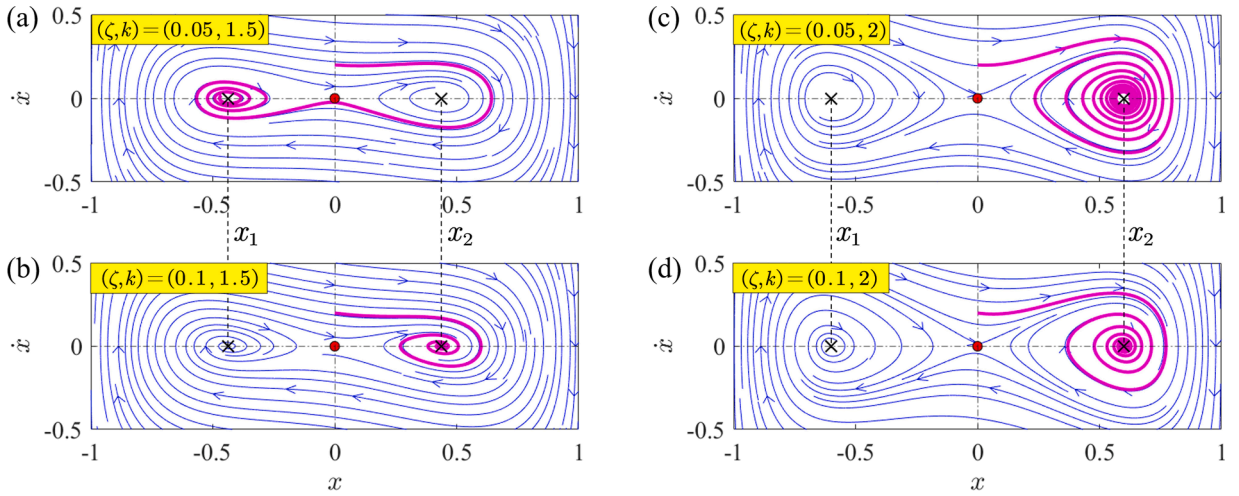


**Fig. 3.** Phase portraits concerning four different $(\zeta, k)$ pairs. Magenta orbits are with the initial condition $(x, \dot{x}) = (0, 0.2)$.

control logic to take these two effects into account,

$$\overline{u}(\overline{t}, \overline{\beta}, \overline{P}, \overline{D}, \overline{\tau}) = \overline{P}(\overline{x}(\overline{t} - \overline{\tau}) - \overline{\beta}) + \overline{D}\dot{\overline{x}}(\overline{t} - \overline{\tau}), \tag{11}$$

where $\overline{P}$ and $\overline{D}$ are the two gains, the parameter $\overline{\tau} > 0$ denotes the inherent delay of the feedback loop due to the inevitable operations such as sensing and data communication; the bias term $\overline{\beta}$ is introduced to specify the desired convergence position so that the feedback force $\overline{u}$ is always nonzero until the two convergence conditions $\overline{x} = \overline{\beta}$ and $\dot{\overline{x}} = 0$ are both achieved. Besides, the parameter $\overline{\tau}$ points out the inevitable controller delay on the one hand, and on the other hand, it provides additional tuning freedom to seek performance enhancement. Plugging (11) into (4), the resulting new dynamics can be reshaped as

$$\begin{cases} \dot{x} = v, \\ \dot{v} = -2\zeta v - F(x) - P(x(t-\tau) - \beta) - Dv(t-\tau), \end{cases} \tag{12}$$

where $P = \overline{P}/\overline{k}_v, D = \overline{D}/(\overline{m}\overline{\omega}_n)$, $\tau = \overline{\tau}\overline{\omega}_n$, and $\beta = \overline{\beta}/\overline{l}$ are dimensionless parameters following (3). Note that we have

$$\begin{cases} \dot{x}(t) = \dot{x}(t-\tau) = 0, \\ \dot{v}(t) = \dot{v}(t-\tau) = 0, \end{cases} \tag{13}$$

in the steady state $t \to \infty$, and therefore when the feedback actuation is activated, the two stable equilibrium points $x_1$ and $x_2$ given in (7) are invariant if we set that $\beta = x_{1,2}$. That is, the considered control logic (11) does not affect equilibria, and tuning $\beta$ allows specifying which equilibrium is effective, i.e., $\beta = x_1$ and $\beta = x_2$ for $x = x_1$ and $x = x_2$, respectively. Furthermore, letting $\beta = 0$ helps activate inter-well motions, which is conducive to ultra-low frequency vibration isolation, as mentioned in [37] and as will be further demonstrated in this work.

### 3.2. Stability criteria

The stability issues of an active BVI must be considered and can be evaluated by the Jacobian matrix of (12),

$$\mathbf{J}_1 = \begin{bmatrix} 0 & 1 \\ -\dfrac{\partial F(x)}{\partial x} - Pe^{-\tau\lambda} & -2\zeta - De^{-\tau\lambda} \end{bmatrix}, \tag{14}$$

where $\lambda$ denotes the characteristic variable, and $\partial F(x)/\partial x = K(x)$ is the stiffness given in Eq. (6). With the bistable condition (8), one can obtain

$$\begin{cases} K_{inter} = K(x = x_0 = 0) = 1 - 2kh < 0, \\ K_{intra} = K(x = x_{1,2}) = \dfrac{(1-2k)(2hk-1)(2k(h-2)+1)}{4k^2(h-1)^2} > 0. \end{cases} \tag{15}$$

Consequently, when $P = D = 0$ (i.e., null feedback actuation), we have $trace(\mathbf{J}_1) = -2\zeta < 0$, and $|\mathbf{J}_1| = K_{inter} < 0$ and $|\mathbf{J}_1| = K_{intra} > 0$ for the equilibrium point $x_0$ and the two $x_1$ and $x_2$, respectively, which agrees with the equilibrium stability determined by the

bistable condition (6). When the feedback actuation is activated, the stability of the BVI is then governed by the characteristic equation

$$CE(\lambda, P, D, \tau, K_{Aux}) = |\lambda \mathbf{I}_{2\times 2} - \mathbf{J}_1| = \lambda^2 + 2\zeta\lambda + K_{Aux} + (P + D\lambda)e^{-\tau\lambda} = 0, \tag{16}$$

where $K_{Aux}$ is an auxiliary variable. Clearly, $K_{Aux} = K_{inter}$ and $K_{Aux} = K_{intra}$ correspond to the BVI operating with inter- and intra-well motions, respectively. From the form of (16), the bias constant $\beta$ does not affect stability. Furthermore, to retain the bistable characteristics when the feedback actuation is activated, the spectrum of

$$CE(\lambda, P, D, \tau, K_{Aux} = K_{intra}) = 0 \tag{17}$$

must have negative real parts for intra-well motions around the two stable equilibria $x_1$ and $x_2$. However, if the BVI is designed to operate with inter-well motions, we require that the associated characteristic equation

$$CE(\lambda, P, D, \tau, K_{Aux} = K_{intra}) = 0 \tag{18}$$

has roots with positive real parts, considering that the BVI tuned with any control parameter composition $(P, D, \tau)$ must be unstable at $x_0$. Otherwise, the convergence at this point leads to no inter-well motions.

**Remark 1**. The stability condition governed by Eq. (17) only applies to the vicinity of the two equilibrium points $x_1$ and $x_2$ since the Jacobian matrix (14) combined with Eq. (15) only considers point stiffness. Consequently, we exclude the cases where the BVI is excited with large external forces so that system dynamics are not within the basins of attraction of the two stable equilibrium points, exemplified by the dynamical flows satisfying $|x| \to 1$ in the phase portraits shown in Fig. 3.

### 3.3. Stability analysis

The aim is to obtain the operable regions of control parameters for tuning the BVI, which now becomes to determine the spectral distributions of the two quasi-polynomial Eqs. (17) and (18).

#### 3.3.1. D-curves and root tendency

D-curves [47], defined as time-domain parameters that correspond to at least one pair of imaginary roots, divide the entire parameter plane into either stable or unstable regions. For this, substituting $\lambda = \pm j\omega_H, \omega_H \geqslant 0$ , where the subscript $(\bullet)_H$ denotes the Hopf bifurcation, into (16) leads to

$$K_{Aux} - \omega_H^2 + j2\zeta\omega_H = -(P + jD\omega_H)e^{-j\tau\omega_H}. \tag{19}$$

Taking the gain $D$ as a constant for operable parameter pairs $(P, \tau)$ (a similar analysis holds when fixing $P$) and denoting the critical parameter pairs constituting the D-curves on the $(P, \tau)$ plane as $(P_c, \tau_c)$, plugging $\omega_H = 0$ into Eq. (19) gives

$$\begin{cases} P_c = -K_{Aux}, \\ 0 \times e^{-j\tau_c \times 0} = 0, \end{cases} \tag{20}$$

which indicates that the critical delay $\tau_c$ can be any real value when $P = -K_{Aux}$ and that Eq. (19) has no definite solutions for $\tau$ when $(P, \omega_H) = (K_{Aux}, 0)$. When $\omega_H > 0$, balancing the real and the imaginary parts of Eq. (19) yields

$$\begin{cases} P_c^2(\omega_H, D, K_{Aux}) = \omega_H^2\left(4\zeta^2 + \omega_H^2 - D^2 - 2K_{Aux}\right) + K_{Aux}^2, \\ \tau_{c,n}(\omega_H, P_c, D, K_{Aux}) = \dfrac{1}{\omega_H}\left[\text{atan2}\left(\dfrac{\omega_H\left[2P_c\zeta + D\left(\omega_H^2 - K_{Aux}\right)\right]}{\omega_H^2(P_c - 2D\zeta) - K_{Aux}P_c}\right) \pm 2(n-1)\pi\right], \end{cases} \tag{21}$$

where $n \in \mathbb{Z}^+$ results from the periodicity of $e^{-j\tau\omega_H \pm j2(n-1)\pi} = e^{-j\tau\omega_H}$, and $\text{atan2}(\cdot) \in [-\pi, \pi]$ is the four-quadrant inverse tangent [48] to match the variety range of the complex exponent $e^{-j\tau\omega_H}$. Note that we have

$$\text{atan2}\left(\frac{0}{-K_{Aux}P_c}\right) = \begin{cases} \pi, K_{Aux}P_c \geqslant 0, \\ 0, K_{Aux}P_c < 0, \end{cases} \tag{22}$$

and thus the critical delay $\tau_{c,n}$ can be arbitrary only when $\omega_H = 0$ and $K_{Aux}P_c < 0$, agreeing with Eq. (20). Remarkably, the value of $\tau_{c,n}$ has two options in the case $\omega_H \to 0_+$, considering that

$$\begin{cases} P_c^{'} = P_c(\omega_H \to 0_+) = P_c(\omega_H = 0) = \pm|K_{Aux}|, \\ \tau_{c,n}(\omega_H \to 0_+) = \dfrac{2P_c^{'}\zeta - DK_{Aux}}{-K_{Aux}P_c^{'}}\left[\lim\limits_{\omega_H^{'}\to 0_+}\dfrac{1}{\omega_H^{'}}\operatorname{atan2}(\omega_H^{'})\right] + \lim\limits_{\omega_H\to 0_+}\dfrac{2(n-1)\pi}{\omega_H} \\ \qquad\qquad = \lim\limits_{\omega_H\to 0_+}\dfrac{2(n-1)\pi}{\omega_H} + \begin{cases} \infty, P_c^{'} = K_{Aux}, \\ \dfrac{-(D+2\zeta)}{K_{Aux}}, P_c^{'} = -K_{Aux}, \end{cases} \end{cases} \tag{23}$$

where $\omega_H^{'} = \omega_H \times (2P_c^{'}\zeta - DK_{Aux})/(-K_{Aux}P_c^{'})$. Hence, when $\omega_H$ varies from $\omega_H = 0$ to $\omega_H = 0_+$, the critical delay $\tau_{c,n}$ converges to a fixed value $\tau_c = (2P_c^{'}\zeta - DK_{Aux})/(-K_{Aux}P_c^{'})$ when $n = 1$ or to infinity $\infty$ when $n > 1$. Given Eqs. (20), (21), and (23), the parameter pairs $(P_c, \tau_c)$ constituting the D-curves can be characterized as

$$\begin{cases} P_c(\omega_H, D, K_{Aux}) = \pm\sqrt{\omega_H^2\left(4\zeta^2 + \omega_H^2 - D^2 - 2K_{Aux}\right) + K_{Aux}^2}, \\ \tau_{c,n}(\omega_H, P_c, D, K_{Aux}) = \begin{cases} Any\ Value, \omega_H = 0, P_c(\omega_H = 0) = -K_{Aux}, \\ Not\ Defined, \omega_H = 0, P_c(\omega_H = 0) = K_{Aux}, \\ \dfrac{1}{\omega_H}\left[\operatorname{atan2}\left(\dfrac{\omega_H\left[2P_c\zeta + D\left(\omega_H^2 - K_{Aux}\right)\right]}{\omega_H^2(P_c - 2D\zeta) - K_{Aux}P_c}\right) \pm 2(n-1)\pi\right], \omega_H > 0. \end{cases} \end{cases} \tag{24}$$

In light of the root continuity rule [47], the characteristic roots shift smoothly on the complex plane as time-domain parameters continuously vary. Therefore, if the number of unstable roots (NU) changes as the pair $(P, \tau)$ varies, it must change at the critical moments when $(P, \tau)$ crosses the D-curves depicted by $(P_c, \tau_c)$. We can then determine the operable parameters.

### 3.3.2. Stability map and operable region

Given a BVI with $(h, k, \zeta) = (0.4, 1.5, 0.05)$, the D-curves $(P_c, \tau_c)$ by sweeping $\omega_H \geqslant 0$ as per (24) in the intra-well case $K_{Aux} = K_{inter} = -0.2$ for $D = 0.05$ are shown as the red curves in Fig. 4(a).

From Fig. 4(a), the D-curves divide the $(P, \tau)$ plane into subregions. Particularly, $P = -K_{inter} = 0.2$ is shown as the dashed line. Note that each point only on this line corresponds to a static root $\lambda = 0$ regardless of the values of $\tau$ as per (24). Besides, such a static root is a fixed root since it is only related to $(P, \omega_H) = (-K_{inter}, 0)$. Furthermore, the convergence of the delay $\tau_{c,n}$ with $n = 1$ to $\tau_c = -(D+2\zeta)/K_{inter} = 0.75$ when $\omega_H$ varies from $\omega_H = 0$ to $\omega_H \to 0_+$ is verified by the intersection point $A$. Since $NU$ only changes when crossing the D-curves, the $NU$ in each sub-region is identical. With the QPmR [49], a numerical tool for calculating the spectrum of a quasi-polynomial equation, we check the $NU$ corresponding to an arbitrary point in each subregion, and the confirmed $NU$ holds for all parameter pairs $(P, \tau)$ in the checked subregion, as marked in Fig. 4(a). One can find that a stable region with $NU = 0$ appears when $P > 0.2$. The equality between the threshold value of $P$ and the reversed stiffness $-K_{inter}$ is guaranteed given that the $P$ term in the PD control (11) functions as a spring with stiffness $P$ when $\tau = 0$. Accordingly, Fig. 4(b) shows the numerical stability map by sweeping

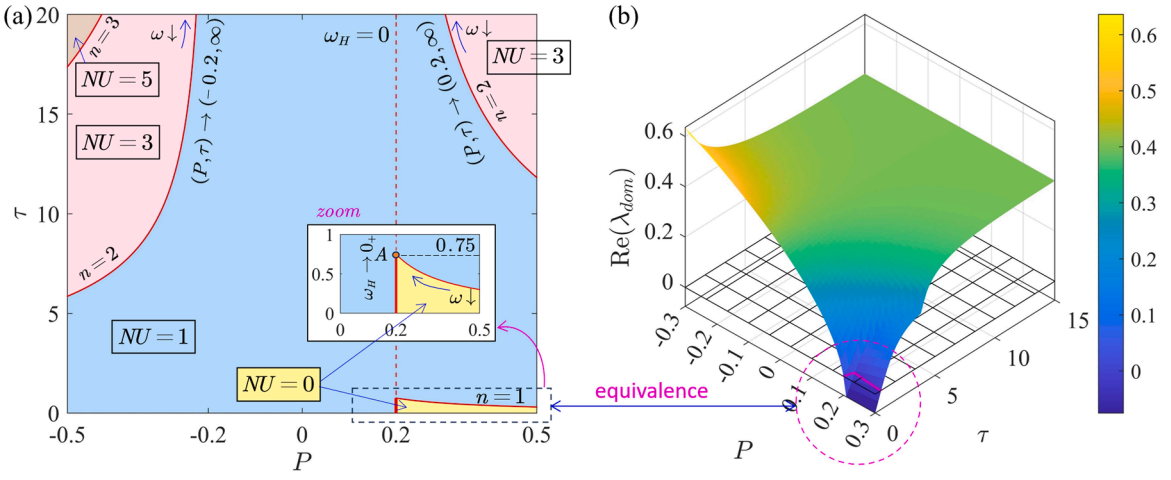


**Fig. 4.** (a). Stability map for inter-well motions with $(h, k, \zeta, D) = (0.4, 1.5, 0.05, 0.05)$. (b). Numerical stability map using QPmR [49]. Grids are with $\mathrm{Re}(\lambda_{\mathrm{dom}}) = 0$, where $\mathrm{Re}(\lambda_{dom})$ means the real part of the rightmost (i.e., dominant) root.

$(P,\tau)$ using QPmR, and the results concur with Fig. 4(a). Hence, operable control parameters for an active BVI operating with inter-well motions should lie outside stable regions.

Following the same procedure, the stability map for the BVI operating with intra-well motions around the two stable equilibrium points $x_1$ and $x_2$ with $K_{intra} = 0.4691$ is shown in Fig. 5(a). This time, the control parameters should render the BVI stable (i.e., $NU = 0$), and the operable ones are marked in yellow. In addition, the blue dashed line corresponds to $\omega_H = 0$. The delay $\tau_{c,1}$ now converges to $\tau_c = -(D+2\zeta)/K_{intra} = -0.3197$ (not shown) as $\omega_H$ varies from $\omega_H = 0$ to $\omega_H \to 0_+$, and we have $\tau_{c,n} \to \infty$ at $P = \pm|K_{intra}|$ when $n > 2$, again verifying (24).

Note that the instability shown in Fig. 4(a) for inter-well motions should be limited around the unstable equilibrium $x_0$. That is, once the active BVI tuned with some control parameter compositions $(P,D,\tau)$ diverges from $x_0$, its dynamics should be captured by the basins of attractions of the two stable equilibria $x_1$ and $x_2$. Otherwise, the overall controlled BVI system is unstable, which would lead to structural failures. Hence, the instability of $x_0$ and the stability of $x_{1,2}$ must simultaneously hold when the feedback actuation is activated. Combining Fig. 4(a) and Fig. 5(a), the operable parameter region is marked in Fig. 5(b). Notably, an active BVI with an unstable equilibrium $x_0$ does not necessarily mean it is practically operable.

### 3.4. Robust parametric range for delay-independent operability

From Fig. 5(b), there exists a parameter region in which an active BVI tuned by any gain $P$ is operable independent of the delay, i.e., the specified delay-independent operability. Clearly, selecting the gain $P$ within this region benefits the robust controller design against delay fluctuations or perturbations [50]. Given the feature that no crossing occurs on D-curves as the delay $\tau$ varies, the aim is to determine the values of $(P,D)$ that make the characteristic Eq. (16) have no imaginary roots $\lambda = \pm j\omega_H$ regardless of $\tau$. To this end, we consider Eq. (19), the magnitude condition of which yields a parabolic equation

$$Q_1(\Omega_H) = \Omega_H^2 + \left(4\zeta^2 - D^2 - 2K_{Aux}\right)\Omega_H + K_{Aux}^2 - P^2 = 0, \tag{25}$$

where $\Omega_H = \omega_H^2$. The axis of symmetry and the discriminant of (25) respectively labeled as $\psi_1$ and $\Delta$ are then governed by

$$\begin{cases} \psi_1 = \dfrac{1}{2}\left(D^2 + 2K_{Aux} - 4\zeta^2\right), \\ \Delta = \left(4\zeta^2 - D^2 - 2K_{Aux}\right)^2 - 4\left(K_{Aux}^2 - P^2\right). \end{cases} \tag{26}$$

Since the zeros $\Omega_H \in \mathbb{R}^+ \cup 0$ of the parabola $Q_1(\Omega_H)$ correspond to the imaginary roots $\lambda = \pm j\omega_H (\omega_H \geqslant 0)$ of (16) and since the parabola opens upwards, we have two cases depending on the location of $\psi_1$ where the parabolic Eq. (25) has no root satisfying $\Omega_H \in \mathbb{R}^+ \cup 0$, i.e., $(i).Q_1(0) > 0$ if $\psi_1 \leqslant 0$; $(ii).\Delta < 0$ if $\psi_1 > 0$, leading to

$$\left\{ (P,D) \middle| \begin{cases} P^2 < K_{Aux}^2, if D^2 \leqslant 4\zeta^2 - 2K_{Aux} \\ P^2 < \dfrac{1}{4}Q_2(D_S), else \end{cases} \right\}, \tag{27}$$

where

$$Q_2(D_S) = -\left(D_S - 4\zeta^2\right)\left(D_S - 4\zeta^2 + 4K_{Aux}\right) \tag{28}$$

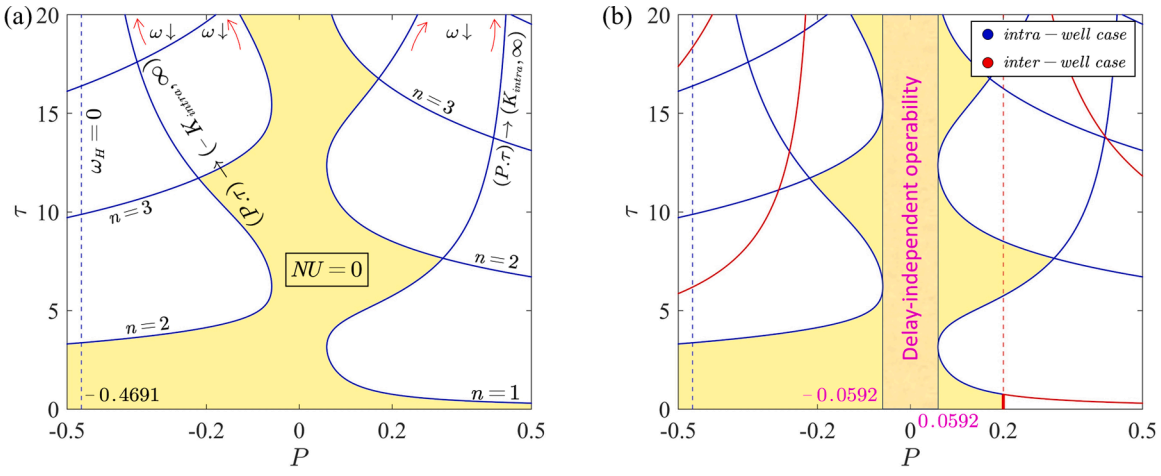


**Fig. 5.** (a). Stability map for intra-well motions with $(h,k,\zeta,D) = (0.4,1.5,0.05,0.05)$. (b). Colored region denotes the operable parameters $(P,\tau)$ for tuning an active BVI. Red and blue curves concur with those in Fig. 4(a) and Fig. 5(a).

is a parabola in $D_S = D^2$ which opens downward. Note that the first inequality $P^2 < K_{Aux}^2$ in (27) corresponds to the self-evident 'delay-independent instability' in the inter-well case, as exemplified in Fig. 4(a), where the BVI is unstable at $x_0$ when $P^2 < 0.2^2$. The second inequality $P^2 < Q_2(D_S)/4$ then correspond to the intra-well case, and it makes sense only if $Q_2(D_S) > 0$. Note also that the axis of symmetry of $Q_2(D_S)$ is $\psi_2 = 4\zeta^2 - 2K_{Aux}$, and we have $\psi_2 \geqslant 0$ in case (*i*) of (27) so that $Q_2(D_S) < Q_2(\psi_2) = 4K_{Aux}^2$ when $D^2 < 4\zeta^2 - 2K_{Aux}$. That is, the operable region governed by the first inequality is covered by that governed by the second one. Thus, Eq. (27) can be combined, yielding the robust region for delay-independent operability

$$\mathbf{\Theta}_{robust} = \left\{ (P, D) \middle| P^2 < \frac{\left(4\zeta^2 - D^2\right)\left(4K_{intra} + D^2 - 4\zeta^2\right)}{4} \right\}, \tag{29}$$

which is a function in $\zeta$ and $K_{intra}$. Selecting the gain pair $(P, D)$ within the robust region $\mathbf{\Theta}_{robust}$, no Hopf bifurcation or stability alternation would occur since no imaginary roots exist or no crossing on D-curves occurs. Considering that the sign of $\psi_2$ determines the maximum of $Q_2(D_S) > 0$ within the interval $D_S > 0$ and that $Q_2(D_S) = 0$ has two zeros $D_{S,1} = 4\zeta^2$ and $D_{S,2} = 4\zeta^2 - 4K_{intra}$ with $D_{S,1} > D_{S,2}$ in light of (15), the lower and upper bounds of the robust region $\mathbf{\Theta}_{robust}$ for the delay-independent operability can be obtained as

$$\begin{cases} |P| \in \left[0, \sqrt{Q_2(0)/4}\right] = \left[0, 2\zeta^2\left(K_{intra} - \zeta^2\right)\right], \\ |D| \in \left[D_{low}, \sqrt{D_{S,1}}\right] = \left[D_{low}, 2\zeta\right], \end{cases} D_{low} = \begin{cases} \sqrt{D_{S,2}}, if\, \zeta^2 > K_{intra}, \\ 0, else. \end{cases} \tag{30}$$

More intuitively, the robust regions $\mathbf{\Theta}_{robust}$ for $k = 1.5$ and different $(\zeta, h)$ values are demonstrated in Fig. 6.

From Fig. 6(a), the robust region $\mathbf{\Theta}_{robust}$ expands in both directions of $P$ and $D$ as damping $\zeta$ increases, indicating that damping is beneficial for suppressing the effects of delay perturbations on system stability. Since $\mathbf{\Theta}_{robust}$ is also related to the stiffness $K_{intra}$ as per (29) and since $K_{intra}$ is a function of $h$, the relationship between $\mathbf{\Theta}_{robust}$ and $K_{intra}$ by varying $h$ is shown Fig. 6(b). The bounds of $P$ and $D$ in both Fig. 6(a) and b) are marked as dashed red curves and agree with ((30). Similar to Fig. 6(a), the maxima of either one of $P$ and $D$ are achieved when the other one is zero, and the difference is that the bounds of $D$ keep invariant when $K_{intra}$ varies. Note that in addition to control robustness, the bound condition $|D| < 2\zeta$ given in (30) and verified in Fig. 6 should be taken as a hard requirement for the BVI design to avoid negative total damping aiming for $|2\zeta\dot{x} + D\dot{x}(t-\tau)| \geq (2\zeta - |D|)|\dot{x}| > 0$ to benefit convergence. For the case $(h,k,\zeta,D) = (0.4,1.5,0.05,0.05)$, the selection of the gain $P$ for delay-independent operability can be found in Fig. 6 to be $P \in [-0.0592, 0.0592]$, which agrees with Fig. 5(b). Notice that Fig. 5(b) and Fig. 6 provide two types of operable regions for selecting the gain pair $(P, D)$ to customize the uses of active BVIs to accommodate different working conditions.

## 4. Delay-coupled bistable dynamics analysis

Having established operable regions for control parameters, we next consider the BVI dynamics under harmonic excitations while considering the delayed feedback actuation (11). The analysis generalizes our recent work [46] where a nondelayed case is considered. Note that the BVI is taken as phase zero to simplify calculations. With the rationalized governing equation, the bistable dynamics, which are complicated by the introduction of delay, including frequency responses and jump frequencies, are determined.

### 4.1. Governing equations and rationalization

In light of [22], the considered harmonic force excitation $\bar{f}$ and base excitation $\bar{x}_b$ are assumed to be

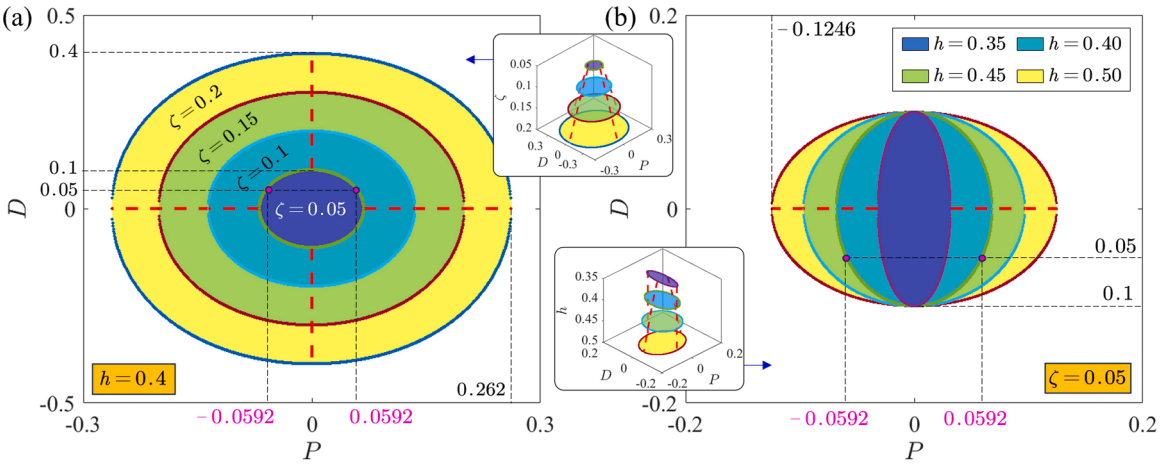


**Fig. 6.** Robust region $\mathbf{\Theta}_{robust}$ governed by (29) for $k = 1.5$. (a). Fixing $h = 0.4$ and varying $\zeta = [0.05, 0.1, 0.15, 0.2]$. (b). Fixing $\zeta = 0.05$ and varying $h = [0.35, 0.4, 0.45, 0.5]$.

$$\begin{cases} \overline{f} = \overline{A}_f cos(\overline{\omega} t + \phi), \overline{A}_f > 0, \\ \overline{x}_b = \overline{A}_b cos(\overline{\omega} t + \phi), \overline{A}_b > 0, \end{cases} \tag{31}$$

where $\overline{A}_f$ and $\overline{A}_b$ are the force and base amplitudes, respectively, and $\phi$ denotes the phase difference between the excitation and the BVI. Proceeding from (12), the BVI dynamics in the force- and base-motion-excited cases are respectively governed by

$$\ddot{x} + 2\zeta\dot{x} + F(x) = -P(x(t-\tau) - \beta) - D\dot{x}(t-\tau) + A_f \cos(\omega t + \phi), \tag{32}$$

$$\ddot{r} + 2\zeta\dot{r} + F(r) = -P(r(t-\tau) - \beta) - D\dot{r}(t-\tau) - A_b\omega^2 \cos(\omega t + \phi), \tag{33}$$

where $A_f = \overline{A}_f/(\overline{k}_v\overline{l})$ and $A_b = \overline{A}_b/\overline{l}$ are self-evident dimensionless excitation amplitudes following (3), $\omega = \overline{\omega}/\overline{\omega}_n$ is the dimensionless excitation frequency, and $r = (\overline{x} - \overline{x}_b)/\overline{l}$ is the relative displacement of the BVI to the base. Particularly, the delayed PD control is based on $r$ in the base-motion-excited case so that Eqs. (32) and (33) share a similar form which can be unified into

$$\ddot{z} + 2\zeta\dot{z} + F(z) = -P(z(t-\tau) - \beta) - D\dot{z}(t-\tau) + A_x\mu \cos(\omega t + \phi). \tag{34}$$

Then, the BVI is subjected to force and base excitations when $(A_x, \mu) = (A_f, 1)$ and $(A_x, \mu) = (A_b, -\omega^2)$, respectively. Note from Eq. (5) that the restoring force $F(z)$ is of an irrational form which complicates dynamical analysis. For simplification, we adopt the [3,3]-order Padé approximation [51] for rationalization, yielding

$$F(z) \approx F_a(z) = \frac{n_1 z + n_2 z^2 + n_3 z^3}{1 + d_2 z^2 + d_3 z^3}, \tag{35}$$

where $n_1 = 1 - 2hk$, $n_3 = [2k(h+2) - 3]/4$, $d_2 = -3/4$, and $n_2 = d_3 = 0$ since $F(z)$ is an odd function. Substituting Eq. (35) into (34) and eliminating the resulting denominator yields the rational governing equation

$$\left(1 + d_2 z^2\right)[\ddot{z} + 2\zeta\dot{z} + P(z(t-\tau) - \beta) + D\dot{z}(t-\tau) - A_x\mu \cos(\omega t + \phi)] + n_1 z + n_3 z^3 = 0, \tag{36}$$

The effectiveness of Eq. (36) for predicting the BVI dynamics exactly governed by Eq. (34) is verified in Section 4.4.

**Remark 2.** The Taylor series, which is widely adopted for rationalization, e.g., [22,23,37], is a reduced case of Padé approximation. Given that a BVI can undergo large-amplitude inter-well motions and that the intra-well motions are not close to the approximation point $z = 0$, the dynamical analysis based on Padé approximation yields a higher accuracy [46]. In addition, the Padé approximation has a better tracking capacity and can work in cases where the Taylor series does not converge [51], which is especially useful in some cases where the original restoring forces can irregularly change [52].

### 4.2. Frequency responses

With the rational form of Eq. (36), the harmonic balance method [53] can now be deployed to investigate the nonlinear BVI dynamics, which are assumed to have the same frequency as the excitation but with a different amplitude $A_z$

$$z(\omega, t) = A_z(t)\cos(\omega t) + B(t), \tag{37}$$

where $A_z(t)$ and $B(t)$ are slow-varying coefficients, and the bias term $B(t) = 0$ and $B(t) \neq 0$ corresponds to the inter- and intra-well motions, respectively. Note that all the time derivatives should vanish in the steady state $t \to \infty$, i.e., $A_z(t) = A_z$ and $B(t) = B$ such that $\ddot{B} = \ddot{A}_z = 0$ and $\dot{B} = \dot{A}_z = 0$. To this end, substituting Eq. (37) into (36), the vanishment of the resulting non-trigonometric terms and the coefficients of the $\sin(\omega t)$ and $\cos(\omega t)$ terms lead to three equations,

$$\begin{cases} G_1(P, D, \tau, \omega, A_z) = A_x\mu \sin(\phi), \\ G_2(P, D, \tau, \beta, \omega, A_z, B) = A_x\mu \cos(\phi), \\ BG_3(P, D, \tau, \beta, \omega, A_z, B) = Bd_2 A_z A_x \mu \cos(\phi), \end{cases} \tag{38}$$

where $G_1$ is a function in $(P, D, \tau, \Omega, A_z)$, and $G_2$, and $G_3$ are additionally in $\beta$. The aim is to seek the common solution composition $(\Omega, A_z, B)$ of Eq. (38) under the bistable condition (8) for a given control parameter composition $(P, D, \tau)$ and a bias constant $\beta$. Since $B = 0$ is a fixed solution of the third equation in (38), the analysis is twofold depending on the value of $B$. Accordingly, the superscripts $(\bullet)^{[1]}$ and $(\bullet)^{[2]}$ respectively denote the inter- and intra-well cases.

#### 4.2.1. Inter-well case with $B = 0$

Let us start with the inter-well case where the BVI can cross the energy barrier $E_b$ to oscillate between the two stable equilibria $x_1$ and $x_2$. Substituting $\beta = B = 0$ into Eq. (38) gives

$$\begin{cases} G_1^{[1]}(\omega, A_z) = (\omega(D\cos(\omega\tau) + 2\zeta) - P\sin(\omega\tau))A_z = A_x\mu\sin(\phi), \\ G_2^{[1]}(\omega, A_z) = \dfrac{1}{\kappa}\left(\kappa[P\cos(\omega\tau) + D\omega\sin(\omega\tau)] + \left(n_3 - d_2\omega^2\right)A_z^2 + \dfrac{4}{3}\left(n_1 - \omega^2\right)\right)A_z = A_x\mu\cos(\phi), \end{cases} \tag{39}$$

where $\kappa = d_2 A_z^2 + 4/3$. To eliminate the terms $\sin(\phi)$ and $\cos(\phi)$, Eq. (39) can be combined as

$$G_3^{[1]}(\omega, A_z) = \left(G_1^{[1]}(\omega, A_z)\right)^2 + \left(G_1^{[1]}(\omega, A_z)\right)^2 - A_x^2\mu^2 = 0, \tag{40}$$

which is an implicit function in $(\omega, A_z)$. Once given an excitation frequency $\omega \in \mathbb{R}^+$, Eq. (40) is a cubic equation in $A_z$

$$G_3^{[1]}(\omega, A_z) = \sum_{i=0}^{3} \alpha_i^{[1]}(\omega) A_z^{2i} = 0, \tag{41}$$

where $\alpha_i^{[1]}$ represents constant coefficients parameterized in $\omega$. Solving $A_z \in \mathbb{R}^+$ from (41) with sweeping $\omega \in \mathbb{R}^+$ leads to the solution pairs $(\omega, A_z)$ for the inter-well frequency response curve $\omega \times A_z$.

**Remark 3.** Solving Eq. (41) for amplitude $A_z$ with sweeping frequency $\omega$ yields two benefits. (*i*). The two terms $\sin(\omega\tau)$ and $\cos(\omega\tau)$ in Eq. (39) or Eq. (41) become two constants for a given delay $\tau$, which converts transcendental equations into simper polynomial ones. (*ii*). Sweeping $\omega$ reduces the number of variables so that Eq. (41) transforms from an implicit equation in $(\omega, A_z)$ to a univariate cubic equation in $A_z$ that can be easily solved. Note that a univariate polynomial equation can be solved by standard procedures regardless of equation degree [54]. Thus, when increasing the approximation order in (35) for higher accuracy, Eq. (41) is always solvable, although it can lead to no closed-form solutions due to higher equation degrees.

#### 4.2.2. *Intra-well case with $B \neq 0$*

Intra-well motions mean that the BVI dynamics are trapped in the basin of attraction of one of the two stable equilibrium points $x_1$ and $x_2$. When $\beta = B \neq 0$, to eliminate the terms $\sin(\phi)$ and $\cos(\phi)$, Eqs. (38) can be combined as

$$\begin{cases} G_1^{[2]}(\omega, A_z, B) = G_1^2(\omega, A_z) + G_2^2(\omega, R, A_z) - A_x^2\mu^2 = 0, \\ G_2^{[2]}(\omega, A_z, B) = G_1^2(\omega, A_z) + G_3^2(\omega, A_z, B) - A_x^2\mu^2 = 0, \\ G_3^{[2]}(A_z, B) = G_2(\omega, A_z, B) - \dfrac{1}{d_2 A_z} G_3(\omega, A_z, B) = 0, \end{cases} \tag{42}$$

where $G_1^{[2]}$ and $G_2^{[2]}$ contain transcendental terms $\cos(\omega\tau)$ and $\sin(\omega\tau)$, and $G_3^{[2]}$ is a polynomial in $(A_z, B)$. Directly solving Eq. (42) using numerical methods is cumbersome. Similar to Eq. (41), treating the pair $(\omega, B)$ known, $G_1^{[2]}$, $G_2^{[2]}$, and $G_3^{[2]}$ are all univariate polynomials in $A_z$, and more specifically, we have

$$\begin{cases} G_1^{[2]}(\omega, A_z, B) = \sum_{i=0}^{6} \alpha_i^{[2]}(\omega, B) A_z^i = 0, \\ G_2^{[2]}(\omega, A_z, B) = \sum_{i=0}^{4} \gamma_i^{[2]}(\omega, B) A_z^i = 0, \\ G_3^{[2]}(\omega, A_z, B) = \sum_{i=0}^{4} \eta_i^{[2]}(\omega, B) A_z^i = 0, \end{cases} \tag{43}$$

where $\alpha_i^{[2]}, \gamma_i^{[2]}$, and $\eta_i^{[2]}$ are coefficients in $(\omega, B)$. However, directly solving $A_z$ from Eq. (43) by sweeping $(\omega, B)$ is still cumbersome since the sweeping range of $B$ is unknown and since we are seeking the common solution of multiple nonlinear equations in this case. To seek the form of a single univariate polynomial equation, which benefits calculations as per Remark 3, we apply the resultant concept [55, 56] following our recent work [46] given the polynomial form of Eq. (43). The computational details are left to [46], and the main idea of eliminating variables is briefly reviewed to demonstrate the simplified calculations by taking the BVI as phase zero, see the forms of Eqs. (31) and (37).

Resultant concept seeks the necessary condition for two polynomial equations to have common solutions. Let us start with $G_2^{[2]} = 0$ and $G_3^{[2]} = 0$ as they have a lower degree. The Sylvester resultant [56] by eliminating $A_z$ is defined as

$$R(\omega,B)=res_{A_z}\left(G_2^{[2]},G_3^{[2]}\right)=\begin{vmatrix}\gamma_4^{[2]} & \gamma_3^{[2]} & \gamma_2^{[2]} & \gamma_1^{[2]} & \gamma_0^{[2]} & 0 & 0 & 0\\ 0 & \gamma_4^{[2]} & \gamma_3^{[2]} & & \cdots & & & 0\\ 0 & 0 & \gamma_4^{[2]} & \gamma_3^{[2]} & & \cdots & & 0\\ 0 & 0 & 0 & \gamma_4^{[2]} & \gamma_3^{[2]} & \cdots & & \gamma_0^{[2]}\\ \eta_4^{[2]} & \eta_3^{[2]} & \eta_2^{[2]} & \eta_1^{[2]} & \eta_0^{[2]} & 0 & 0 & 0\\ 0 & \eta_4^{[2]} & \eta_3^{[2]} & & \cdots & & & 0\\ 0 & 0 & \eta_4^{[2]} & \eta_3^{[2]} & & \cdots & & 0\\ 0 & 0 & 0 & \eta_4^{[2]} & \eta_3^{[2]} & \cdots & & \eta_0^{[2]}\end{vmatrix}, \tag{44}$$

which is a polynomial in a single variable $B$, where the notation $res_{A_z}(\cdot)$ signifies the resultant operation to eliminate $A_z$. Besides, necessary condition means that all solutions $B$ in the common solutions $(A_z,B)$ of $G_2^{[2]}=0$ and $G_3^{[2]}=0$ belong to the solution set of the univariate resultant equation

$$R(\omega,B)=B^{12}\sum_{i=0}^{16}\vartheta_i^{[2]}(\omega)B^i=0, \tag{45}$$

where $\vartheta_i^{[2]}(\omega)$ denotes constant coefficients once given a frequency $\omega$. Since $B\neq 0$, Eq. (45) has 16 real solutions at most, back substituting each of which into $G_2^{[2]}=0$ or $G_3^{[2]}=0$ yields a univariate equation in $A_z$, and therefore $A_z$ can be solved. To this end, we can now obtain all the common solution candidates $(A_z,B)$ of $G_2^{[2]}=0$ and $G_3^{[2]}=0$ for a given frequency $\omega$. Note that the term 'candidates' highlights that the resultant concept only provides necessary conditions for common solutions, i.e., the common solution pairs $(\omega,B)$ of $G_2^{[2]}=0$ and $G_3^{[2]}=0$ for any value of $A_z$ must satisfy the resultant Eq. (45), but the opposite is not always the case. Considering also that the feasible solution composition $(\omega,A_z,B)$ must additionally satisfy $G_1^{[2]}=0$, all these solution candidates need to be checked twice to obtain the desired common solutions of Eq. (43), and the corresponding computational procedure by sweeping the frequency $\omega$ is detailed in Fig. 7.

From Fig. 7, the common solution composition $(\omega,A_z,B)$ is determined via two solving steps and two checking steps. Note that each solving step deals with a purely univariate polynomial equation, and thus solutions of each equation can be exhaustively determined using standard procedures without initial guesses, as also mentioned in Remark 3. Comparing Fig. 7 and Fig.6 of [46], one can conclude that the resultant operations herein are reduced twice and the solving steps are reduced by one since taking BVI as phase zero reduces the number of variables, which improves calculation efficiency. The corresponding numerical comparisons are prepared in Section 4.4.

**Remark 4.** (Implementation of Fig. 7)**.** The resultant operation performed in (44) and Fig. 7 can be easily implemented in mathematical software, e.g., the considered Sylvester resultant concept is embedded into the command *resultant*$(\cdot)$ in the widely used MATLAB, MAPLE, and Mathematica. Besides, the command *roots*$(\cdot)$ of MATLAB and MAPLE and the one *NRoots*$(\cdot)$ of Mathematica can be used to solve a univariate polynomial equation. Hence, once the three governing equations in (42) for intra-well frequency responses are constructed via the harmonic balance method, the introduction of the resultant concept for solving equations does not pose additional programming complexities.

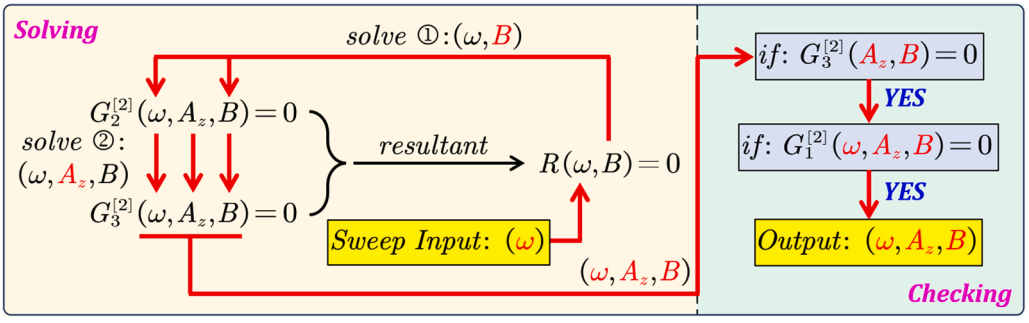


**Fig. 7.** Resultant-based frequency-sweeping solving procedure for intra-well frequency responses. Red arrows and symbols denote the solving flow and main variables, respectively.

### 4.3. Jump frequency

Jump frequency is a key dynamical index of nonlinear systems. It is related to the multi-state frequency band and signifies the critical frequencies where system dynamics can suddenly change even if the excitation frequency slowly varies.

#### 4.3.1. Inter-well case with $B = 0$

For the inter-well motions, we consider the differential form of Eq. (40) in terms of the amplitude $A_z$,

$$\frac{\partial G_3^{[1]}(\omega, A_z)}{\partial A_z} = \frac{\partial G_3^{[1]}(\omega, A_z)}{\partial A_z} + \frac{\partial G_3^{[1]}(\omega, A_z)}{\partial \omega}\frac{\partial \omega}{\partial A_z} = 0. \tag{46}$$

Since the jump frequencies satisfy $\partial\omega/\partial A_z = 0$ as per [13], Eq. (46) at the jump frequencies can then be simplified into

$$\frac{\partial G_3^{[1]}(\omega, A_z)}{\partial A_z} = 0, \tag{47}$$

which is a polynomial equation in $A_z$ as per (41). Consequently, jump frequencies if exist must be the solutions of

$$G_4^{[1]}(\omega) = res_{A_z}\left(G_3^{[1]}(\omega, A_z), \frac{\partial G_3^{[1]}(\omega, A_z)}{\partial A_z}\right) = 0, \tag{48}$$

which is a transcendental equation in a unique variable $\omega$ and can be numerically solved. Compared to Theorem 5 of [46], only one resultant procedure is now required to arrive at (48) thanks to the reduced number of variables by taking the BVI dynamics as phase zero, thus simplifying the calculations.

#### 4.3.2. Intra-well case with $B \neq 0$

For jump frequencies of intra-well responses, the resultant-based calculations in Theorem 6 of [46] also hold and can be simplified similarly to (48). Alternatively, we provide a numerical approach that does not depend on the resultant procedure for comparisons. According to Fig. 7 of [46], the intra-well amplitude can jump at the bending of both the frequency response curves $\omega \times A_z$ and $\omega \times B$. We then seek the extremal condition of the frequency $\omega$ concerning $A_z$ and $B$,

$$\frac{\partial \omega}{\partial A_z} = 0 \ and \ \frac{\partial \omega}{\partial B} = 0, \tag{49}$$

which leads to (47) in the reduced inter-well case with $B = 0$. Furthermore, Eq. (49) can be rewritten as

$$d\omega = \frac{\partial \omega}{\partial A_z}dA_z + \frac{\partial \omega}{\partial B}dB = 0. \tag{50}$$

To seek the form of (50), we consider the derivatives of the first two equations in (42),

$$\begin{cases} \dfrac{\partial G_1^{[2]}(\omega, A_z, B)}{\partial A_z}dA_z + \dfrac{\partial G_1^{[2]}(\omega, A_z, B)}{\partial B}dB = -\dfrac{\partial G_1^{[2]}(\omega, A_z, B)}{\partial \omega}d\omega, \\ \dfrac{\partial G_2^{[2]}(\omega, A_z, B)}{\partial A_z}dA_z + \dfrac{\partial G_2^{[2]}(\omega, A_z, B)}{\partial B}dB = -\dfrac{\partial G_2^{[2]}(\omega, A_z, B)}{\partial \omega}d\omega. \end{cases} \tag{51}$$

Substituting (50) into (51) leads to the matrix equation

$$\mathbf{J}_2\begin{bmatrix} dA \\ dB \end{bmatrix} = 0, \tag{52}$$

which has solutions only if the matrix $\mathbf{J}_2$ is singular, yielding the explicit form of the two extremal conditions in (49)

$$G_4^{[2]}(\omega, A_z, B) = |\mathbf{J}_2| = \begin{vmatrix} \dfrac{\partial G_1^{[2]}}{\partial A_z} & \dfrac{\partial G_1^{[2]}}{\partial B} \\ \dfrac{\partial G_2^{[2]}}{\partial A_z} & \dfrac{\partial G_2^{[2]}}{\partial B} \end{vmatrix} = 0. \tag{53}$$

Combining Eq. (53), $G_3^{[2]}(A_z, B) = 0$, and either one of $G_1^{[2]}(\omega, A_z, B) = 0$ and $G_2^{[2]}(\omega, A_z, B) = 0$, the compositions $(\omega, A_z, B)$ at the jump frequencies can be numerically determined. One benefit of calculations using (53) is that the resulting common solution does not require the checking steps as in Fig. 7. However, solving multiple variables from multiple equations requires a proper solving interval or initial guess to benefit convergence. Instead, the convergence of the resultant-based procedure to construct Eq. (48) is guaranteed thanks to the univariate solving procedure. We also remark that these benefits can be more dominant when $\tau = 0$ so that the equations to be solved for jump frequencies are purely polynomial.

### 4.4. Case studies

Given a BVI with $(h, k, \zeta) = (0.4, 1.5, 0.05)$, two stable equilibrium points $z_{1,2} = \mp 0.4359$ exist as per (7). The harmonic force excitation with $A_f = 0.015$ is then applied to the proof mass, and the resulting numerical dynamics and the associated theoretical solutions for three parameter compositions $(P, D, \tau)$ are compared in Fig. 8.

The numerical solutions shown as magenta and green solid curves in Fig. 8 depict the BVI dynamics governed by the exact restoring force (5), which are derived using the 4th-order Runge-Kutta method with a slow forward frequency sweeping rate to suppress the interferences of adjacent frequency responses. Moreover, theoretical response curves in blue and black markers are obtained as per Section 4.2, and dashed lines corresponding to the bends of frequency response curves are determined following Section 4.3 for jump frequencies. Clearly, theoretical predictions agree with numerical solutions.

We have $\beta = z_1$ in Fig. 8(a-c) to activate intra-well motions so that the proof mass cannot escape from the potential well at $z_1$, yielding oscillations around this point. Comparing the three subplots in Fig. 8(a-c), one can conclude that the delayed PD control logic does not change equilibrium while it affects oscillation amplitudes, thus leading to possible enhanced vibration isolation. Furthermore, the intra-well frequency response curves bend to the left, signifying softening stiffness.

We next lower the energy barrier $E_b$ by reducing $h$ as per Fig. 2(b) while increasing the excitation strength for inter-well motions. Letting $(h, A_f) = (0.35, 0.08)$ leads to two new equilibrium points $z_{1,2} = \mp 0.2222$, thus arriving at Fig. 8(d-f), where numerical dynamics and theoretical solutions are still in good agreement. In the passive case shown in Fig. 8(d), the BVI first undergoes inter-well motions and then oscillates in the potential well at $z_2 = 0.2222$, indicating that low-frequency excitations are prone to cause inter-well motions. When the feedback actuation is activated in Fig. 8(e) and (f), the BVI crosses the unstable equilibrium point $z_0$ as expected while undergoing large- and small-amplitude inter-well motions in low- and high-frequency bands, respectively. The amplitude diversity depending on excitation frequency is qualitatively determined in Section 5.3.4. Note from Fig. 8(c) and (f) that the often-overlooked loop delay can significantly alter dynamical behaviors, making it worthy of being considered as an effective tunable control parameter to enhance vibration isolation performance.

On the other hand, comparing Fig. 8(a-c) and (d-f), the BVI exhibits hardening and softening stiffness characteristics when undergoing intra- and inter-well motions, respectively. This is different from the conventional monostable vibration isolators that only have a single stiffness characteristic. The switching mechanism of BVI between hardening and softening stiffness can be interpreted from a practical perspective. Since $z_0 = 0$ is unstable, dynamics departing from it are stabilizing, leading to hardening stiffness. As for intra-well motions around $z_{1,2}$, the restoring force by the two horizontal springs $\bar{k}_h$ and that by the vertical one $\bar{k}_v$ are competing and are balanced at $z_{1,2}$. Hence, when $z \neq z_{1,2}$, one restoring force is always partially offset by the other one, resulting in softening stiffness. Clearly, the considered feedback actuation facilitates the BVI switch between intra- and inter-well motions or between the softening and the hardening stiffness.

**Remark 5**. We highlight the improved efficiency of the resultant-based solving procedure in Fig. 7 by taking the BVI as phase zero.

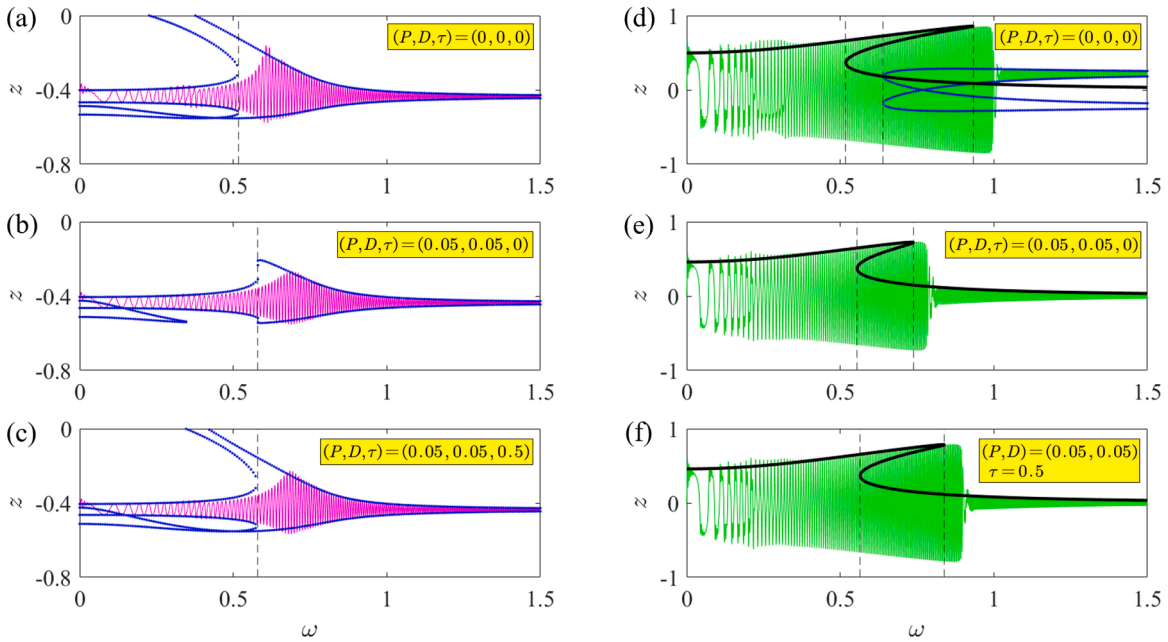


**Fig. 8.** Comparisons between numerical dynamics (magenta and green solid curves) and theoretical solutions (blue and black markers). (a-c). Intra-well motions with $(h, A_f) = (0.4, 0.015)$. (d-f). Inter-well motions with $(h, A_f) = (0.35, 0.08)$. Initial conditions in the intra-well and inter-well cases are set as $(z, \dot{z}) = (z_1, 0)$ and $(z, \dot{z}) = (0, 0)$, respectively.

The frequency interval $\omega \in [0, 1.5]$ of Fig. 8 is linearly divided into 200 grids following our previous work [46], and the average computational time for the intra-well response curves shown in Fig. 8(a-c) is less than 0.25 s using the identical hardware and software resources to [46]. As for the inter-well cases in Fig. 8(d-f), the average time cost is less than 0.1 s. However, similar results for the intra- and inter-well motions given in Table 1 of [46] require much longer time costs of 30 s and 11 s, respectively, although previous results did not consider the delay effect. The significantly saved computational costs extend the application of Padé approximation and resultant concept in nonlinear dynamics analysis for higher efficiency and accuracy.

## 5. Enhanced vibration isolation performance

We next evaluate the vibration isolation performance of the active BVI under harmonic force and base excitations to show how to properly tune the delayed feedback actuation to enhance performance. The special strength of the BVI operating inter-well motions in handling ultra-low-frequency excitations is qualitatively investigated.

### 5.1. Force transmissibility

The total force transmitted from the proof mass to the base through the springs, the damper, and the feedback actuation is

$$F_T = 2\zeta\dot{z} + F(z) + P(z(t-\tau) - \beta) + D\dot{z}(t-\tau). \tag{54}$$

According to [12], if the proof mass is excited by a harmonic force $f = A_f\cos(\omega t + \phi)$, the resulting total force (54) can be approximated by a harmonic form of

$$F_T = A_T\cos(\omega + \phi_T), \tag{55}$$

where $A_T$ is the amplitude and $\phi_T$ is the phase difference with respect to the proof mass. Eq. (54) has a similar form to (34) and thus can also be solved by the harmonic balance method, leading to three equations similar to Eq. (38) as

$$\begin{cases} G_{T1}(\omega, A_z) = (\omega(D\cos(\omega\tau) + 2\zeta) - P\sin(\omega\tau))A_z = A_T\sin(\phi_T), \\ G_{T2}(\omega, A_z, B) = \dfrac{1}{\kappa_T}\left(\kappa_T[P\cos(\omega\tau) + D\omega\sin(\omega\tau)] + \left(n_3 - d_2\omega^2\right)A_z^2 + \dfrac{3}{4}n_3\left(B^2 + A_z^2\right) + n_1\right)A_z = A_T\cos(\phi_T), \\ BG_{T3}(\omega, A_z, B) = BA_zA_Td_2\cos(\phi_T), \end{cases} \tag{56}$$

where $\kappa_T = 1 + (B^2 + 3A_z^2/4)d_2$, and $G_{T3}$ is a function in $(\omega, A_z, B)$. The force transmissibility, defined as the amplitude ratio between the force transmitted to the base and the force excitation, can then be obtained

$$T_f(\omega, A_z, B) = \frac{|F_T|}{|f|} = \frac{A_T(\omega, A_z, B)}{A_f} = \frac{\sqrt{G_{T1}^2 + G_{T2}^2}}{A_f}, \tag{57}$$

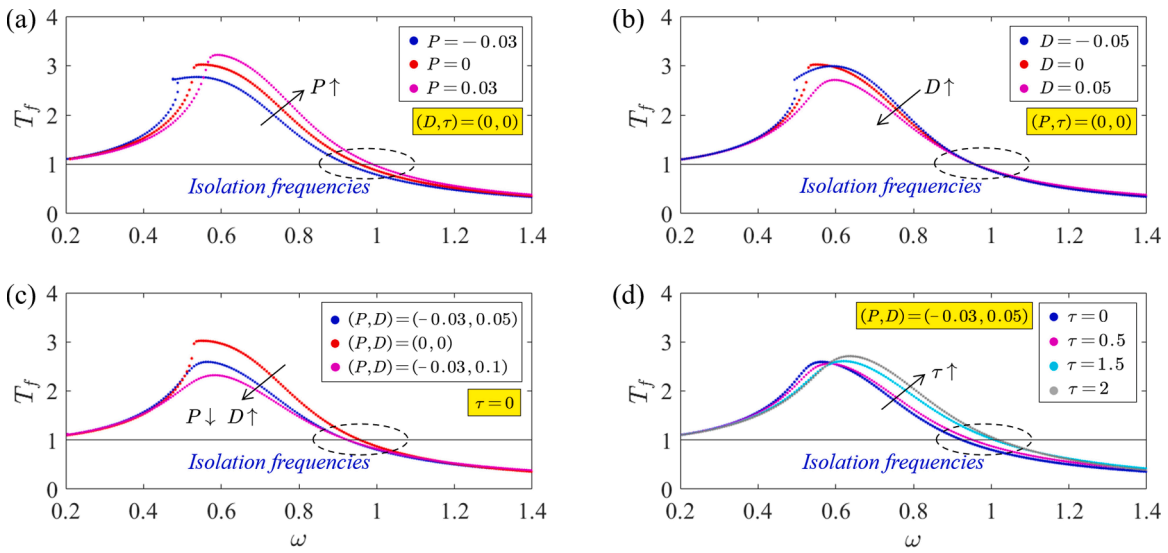


**Fig. 9.** Force transmissibility of the active BVI versus various control parameter compositions. The non-delayed cases are shown in subplots (a), (b), and (c), and the delay effects are considered in subplot (d).

which is a function related to frequency responses governed by Eq. (38). Selecting $(h,k,\zeta) = (0.4, 1.5, 0.1)$, the performance of the active BVI operating with intra-well motions under harmonic force excitations with amplitude $A_f = 0.018$ for various control parameter compositions is compared in Fig. 9.

First, the control parameter compositions $(P,D,\tau)$ should be selected as per Fig. 5(b) or Fig. 6 for stability or robustness. Let us then start with the non-delayed cases in Fig. 9(a-c) to focus on the effects of the two gains $P$ and$D$. From Fig. 9(a), when the feedback actuation is inactive (i.e., $(P,D)$=(0,0)), the isolation frequency is much smaller than $\sqrt{2}$ and the peak frequency is smaller than 1, signifying that the BVI exhibits HSLDS characteristics. Besides, the transmissibility curves bending to the left imply the softening stiffness, which benefits broadband vibration isolation [37]. Of interest is that increasing the gain $P$ worsens the isolation performance by raising the peak amplitude and narrowing the isolation region, although it introduces an additional stiffness around the equilibrium to suppress small perturbations. Besides, decreasing $P$ yields the opposite results to benefit vibration isolation performance, while the transmissibility in the low-frequency band undesirably rises. Fixing $P = 0$ and varying the gain $D$ lead to Fig. 9(b), where the isolation band does not depend much on $D$, while the peak amplitude can be suppressed by raising $D$. Combining such benefits resulting from a negative gain $P$ and a positive $D$ arrives at Fig. 9(c), where the active BVI exhibits a lower peak amplitude and a broadened isolation band compared with the passive BVI with $(P,D)$=(0,0). In addition, the undesirably raised transmissibility in the low-frequency mentioned in Fig. 9(a) can also be suppressed. At last, Fig. 9(d) shows the delay effects on vibration isolation, where the peak amplitude first decreases and then increases as $\tau$ enlarges. Meanwhile, the isolation frequency keeps increasing.

### 5.2. Displacement transmissibility

Now let the base undergo harmonic motions prescribed by $x_b = A_b\cos(\omega t + \phi)$, and the BVI is designed to reduce the resulting vibrations on the proof mass. From Eq. (33), the absolute displacement of the proof mass is

$$r + x_b = A_z\cos(\omega) + A_b\cos(\omega t + \phi). \tag{58}$$

Then, the isolation performance is evaluated by the displacement transmissibility, which depicts the amplitude ratio between the absolute displacement of proof mass and base,

$$T_d(\omega, A_z, B) = \frac{|r + x_b|}{|x_b|} = \frac{\sqrt{A_z^2 + A_b^2 + 2A_zA_b\cos(\phi)}}{A_b}, \tag{59}$$

where $\cos(\phi)$ is defined in Eq. (38). For harmonic base excitations with $A_b = 0.018$, the displacement transmissibility of the BVI operating with intra-well motions and $(h,k,\zeta) = (0.4, 1.5, 0.05)$ for various control parameters is compared in Fig. 10.

From Fig. 10, the beneficial HSLDS characteristics and softening stiffness can also be observed in the base-excited case. Besides, the parametrical effects of $(P,D,\tau)$ on the displacement transmissibility are similar to the force excitation cases in Fig. 9, i.e., a negative gain $P$ extends the isolation band and a positive gain $D$ suppresses the peak amplitude, and such two benefits can take effect simultaneously as in Fig. 10(c). As for the delay effects shown in Fig. 10(d), slightly increasing the delay $\tau$ suppresses the peak amplitude while posing little effect on the isolation band, and similar results can also be found in Fig. 9(d). That is, tuning or actively introducing a delay $\tau$ within a reasonable value in the feedback loop is equivalent to a beneficial damping effect. This provides a useful guideline for

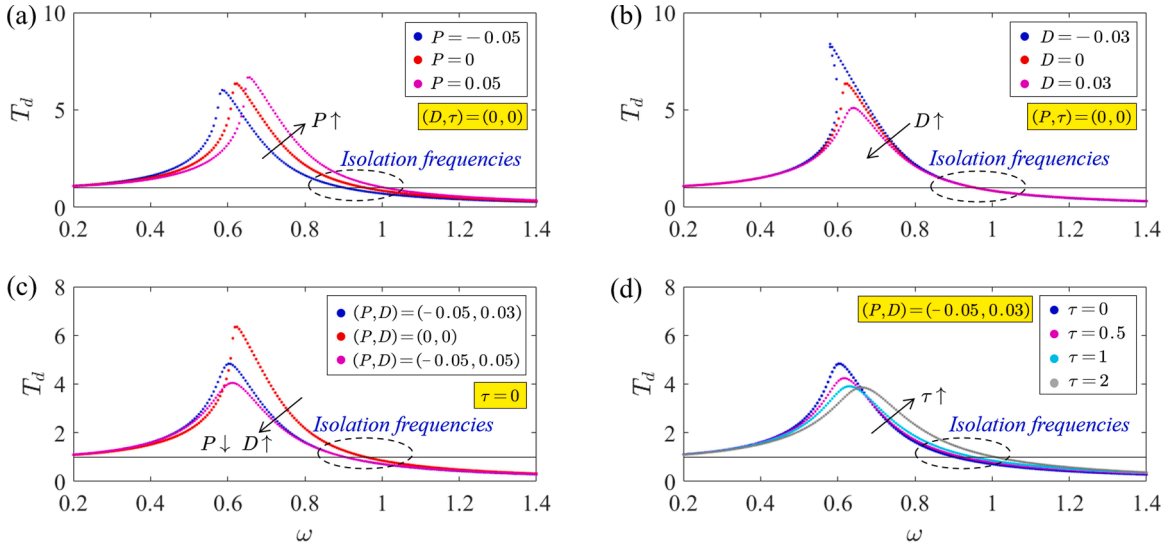


**Fig. 10.** Displacement transmissibility of the active BVI versus various control parameter compositions $(P,D,\tau)$. The non-delayed cases are shown in subplots (a), (b), and (c). The delay effects are evaluated in subplot (d).

the economical feedback loop design in some cases where the loop delay cannot be ignored, e.g., the physical installation distance between the actuator and controller is not close for controller protection purposes, a large number of calculations or signal processing is needed for a large-scale isolator net, etc. Note also that the robust interval $\mathbf{\Theta}_{robust}$ defined in (29) for the gain pair $(P, D)$ becomes more important in these scenarios.

### 5.3. Highlights: ultra-low-frequency vibration isolation using inter-well motion

We have shown that BVIs operating with intra-well motions exhibit HSLDS characteristics yielding broadband vibration isolation, which, in fact, can also be achieved by conventional QZS isolators. We next consider the special benefits of the BVI operating with its exclusive inter-well motions, which are observed to contribute to isolating ultra-low-frequency base vibrations in our previous works [35–37]. As a further step, how the BVI enters such an isolation state, challenges of practically achieving such benefits, tuning rules of the feedback actuation, and the mechanism of isolation valley are highlighted in this study.

#### 5.3.1. Passive BVI

Selecting $(k, h, \zeta) = (6.5, 0.08, 0.1)$ leads to two stable equilibrium points as $r_{1,2} = x_{1,2} = \mp 0.0816$. For $A_b = 0.15$, frequency responses of the BVI and the associated displacement transmissibility are depicted in Fig. 11(a) and (b), respectively. Besides, bifurcation diagrams in such two subfigures are composed of numerical local maxima after a sufficiently long simulation time, and obviously, numerical results agree well with theoretical solutions.

From Fig. 11(a) and Fig. 11(b), the proof mass starts with intra-well motions and then undergoes inter-well motions with large-amplitude aperiodic dynamics (LAAD) [57] as the excitation frequency $\omega$ increases. The LAAD frequency band should be avoided since the amplitudes of the proof mass in this band are larger than the excitation amplitude, and irregular motions can lead to structural fatigue more easily, see Fig. 11(c) for a quasi-periodic example at $\omega = 0.12$. After the LAAD band, an isolation valley where $T_d < 1$ appears, and we can find that the motion amplitude of the proof mass converges and the motions tend to be periodic as $\omega$ increases in the isolation valley. Furthermore, the isolation performance at two frequencies $\omega = 0.14$ and $\omega = 0.15$ within the valley is illuminated in Fig. 11(d), where both amplitudes of absolute displacement and absolute velocity of the proof mass are smaller than those of the base, thus verifying the effective vibration isolation.

Note that inter-well motions constitute the isolation valley, and conventional linear isolators (isolation frequencies are always larger than $\sqrt{2}$) and nonlinear QZS isolators are unable to achieve such ultra-low-frequency vibration isolation. For comparisons, we let $k = 6.25$ so that $K(x = 0) = 0$ as per (6) to construct a QZS isolator, and the associated displacement transmissibility is superposed as the cyan dotted curves in Fig. 11(b), where the superiority of the BVI for the ultra-low-frequency vibration isolation can be easily observed. More specifically, the corresponding numerical phase portraits at $\omega = 0.15$ are compared in Fig. 11(d), where the QZS isolator yields no vibration isolation and even undesirably amplifies the base motion amplitude on the proof mass. As $\omega$ further increases, no intra-well solution exists, and the BVI undergoes pure inter-well motions. However, utilizing inter-well motions to achieve ultra-low-frequency vibration isolation is not easy as the valley width is quite narrow. Consequently, small excitation frequency mismatches can reduce isolation performance or even lead to the LAAD modes. That is, the operating modes of a passive BVI to achieve the isolation valley can be very limited in practice.

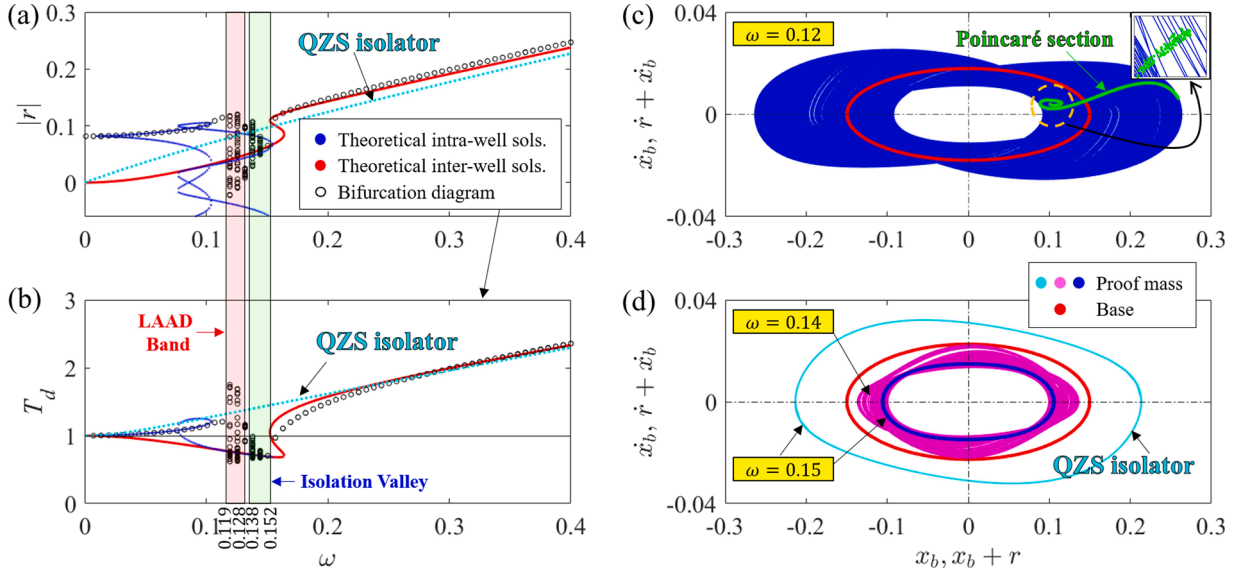


**Fig. 11.** Passive BVI performance with $(P, D, \tau) = (0, 0, 0)$. (a). Frequency responses. (b). Displacement transmissibility. (c). Phase portraits of the motions at $\omega = 0.12$. (d). Ultra-low frequency vibration isolation at $\omega = [0.14, 0.15]$.

*5.3.2. Tunable isolation valley by deploying an active BVI*

Delayed feedback actuation is now activated to enhance the ultra-low-frequency vibration isolation. Given the robust region (29) and the beneficial effect of a positive gain $D$ revealed in Fig. 9 and Fig. 10, we select $P = [\pm 0.01, \pm 0.02]$ and $D = [0, 0.03]$. Similar to Fig. 9 and Fig. 10, we start with the non-delayed cases. The displacement transmissibility for low-frequency harmonic base excitations with $A_b = 0.15$ concerning various gain pairs $(P, D)$ are compared in Fig. 12.

Let us first scrutinize the left four subplots (a-d) of Fig. 12. From Fig. 12(a) and (b), decreasing the stiffness around the equilibrium point $r = 0$ by a negative gain $P$ shifts the isolation valley rightward, which also makes this point more unstable such that the LAAD modes exhibit higher amplitudes and the isolation performance reduces in the valley. In contrast, increasing the gain $P$ leads to Fig. 12 (c) and (d), where the amplitudes of the LAAD modes are suppressed, and the isolation valley shifts leftward with a reduced depth. The effects of the gain $D$ are investigated in Fig. 12(e-h), indicating that increasing $D$ extends the valley width and enhances the isolation performance in the valley. Note that pure periodic motions in the isolation valley protect the proof mass from both perspectives of lower displacement transmissibility and regular motions. Hence, the isolation valley can be considerably extended and its position can be manipulated by properly tuning the gain pair $(P, D)$ in real-time, as marked in Fig. 12(e-h). Moreover, compared to a passive BVI, the active one tuned with a positive gain $D$ exhibits beneficial lower transmissibility in the resonance region. Compared to the conventional QZS isolators, the extended isolation valley means more apparent strength of an active BVI on isolating the ultra-low-frequency

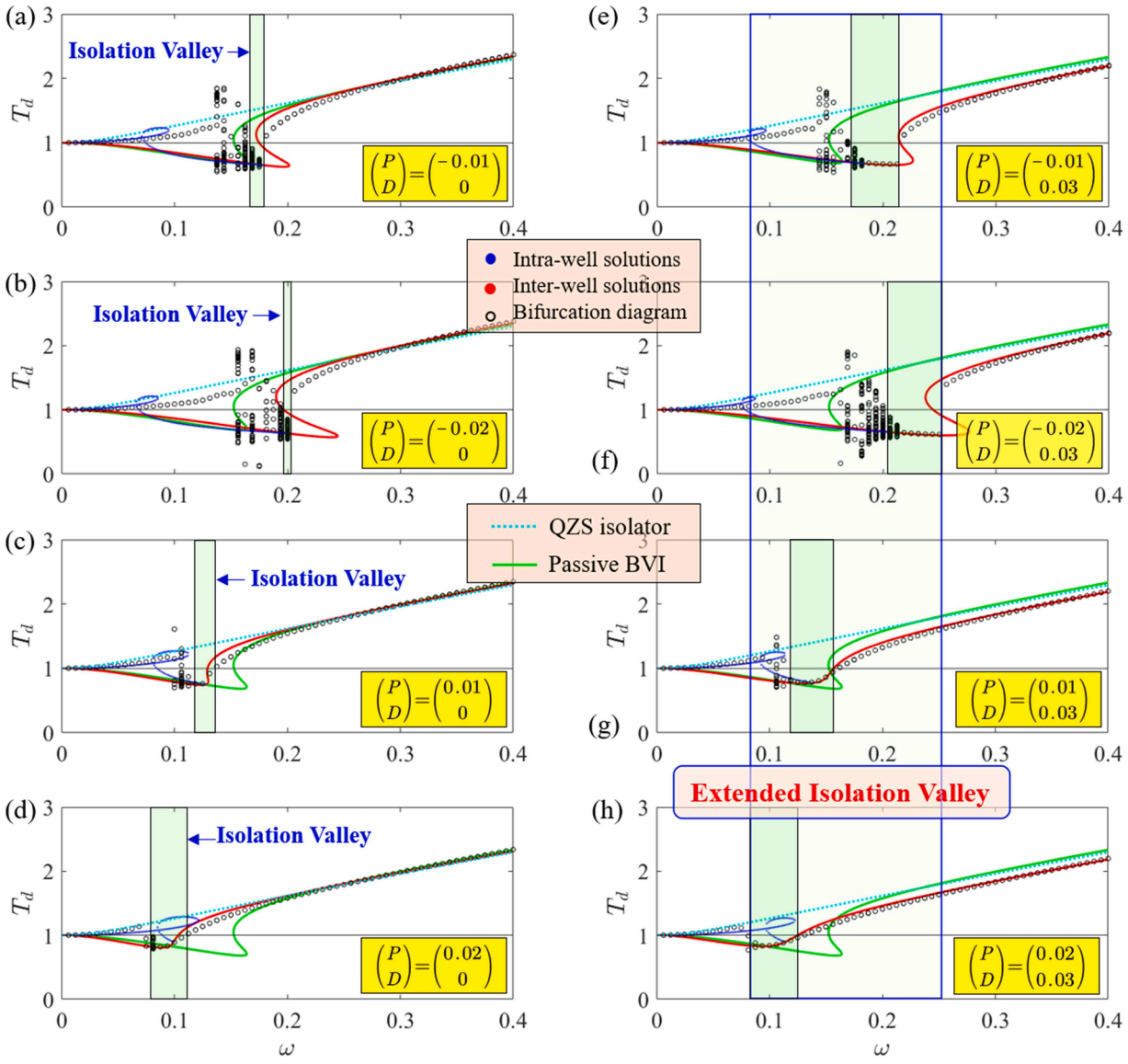


**Fig. 12.** Displacement transmissibility of the active BVI tuned with various pairs of $(P, D)$ and free delay $\tau = 0$ for ultra-low-frequency vibration isolation. The isolation valley is marked as green bands.

vibration. Furthermore, the revealed benefits of tuning $(P, D)$ on isolation valley signify the mechanical design principles of a practical BVI, considering that the gain pair $(P, D)$ is equivalent to a spring plus a damper when $\tau = 0$, see Section 3.1.

The delay effects are evaluated in Fig. 13. Comparing Fig. 13(a-b) and Fig. 12(f), one can conclude that, for a negative gain $P$, increasing the delay $\tau$ shifts the isolation valley rightward, suppresses the aperiodic dynamics and extends the valley width. Therefore, the delay $\tau$ in this case functions as the roles of both the two gains $P$ and $D$. Besides, the delay effects in the cases where the gain $P$ is positive are shown in Fig. 13(c-d). Comparing such two figures and Fig. 12(h) shows that increasing $\tau$ shifts the isolation valley leftward with narrowing the width and undesirably raises the transmissibility in the resonance region. That is, increasing $\tau$ produces the same effect as the gain $P$ while the opposite effect as the gain $D$. Consequently, for an active BVI operating with inter-well motions, the fast-response requirements of the controller can be relaxed when $P < 0$, and the controller delay even benefits the isolation performance. However, the delay effects deserve more attention if we tune $P > 0$ aiming to enhance the ultra-low-frequency vibration isolation by further lowering the isolation frequency, especially when the practical isolation performance does not agree well with the theoretical prediction due to the narrow valley width.

### 5.3.3. *Qualitative analysis of ultra-low-frequency vibration isolation by isolation valley*

With Fig. 11, Fig. 12, and Fig. 13, we next qualitatively investigate the mechanism of ultra-low-frequency vibration isolation by a BVI operating with inter-well motions. In the base-motion-excited case, dynamics of the proof mass of a passive vibration isolator are governed by the forces produced by the damper $\bar{c}$ and the spring composition $(\bar{k}_v, \bar{k}_h, \bar{k}_h)$, see Fig. 1. Furthermore, note from Eq. (59) that effective vibration reduction $T_d < 1$ necessitates that

$$\cos(\phi) < -\frac{A_z}{2A_b} \mapsto \phi \in \left(\frac{\pi}{2}, \pi\right). \tag{60}$$

For conventional passive linear and HSLDS vibration isolators, which have a single stable equilibrium point at $r = 0$ and $F(|r|) > 0$ around $r = 0$, the relationship between the phase difference $\phi$ and the forces exerted on the proof mass in the low-frequency case $\omega \ll 1$ is shown in Fig. 14(a), where dimensional forces are considered.

The angle $\theta$ in Fig. 14(a) is related to the nonlinear restoring forces caused by horizontal springs $\bar{k}_h$, i.e., $\theta = 0$ when $k = 0$, and $\theta \to 0$ when $\omega \to 0$ and $|d_2\bar{r}^2| \ll 1, |n_3\bar{r}^3| \ll |n_1\bar{r}|$. Moreover, the angle $\theta'$ signifies the phase difference between $\bar{x}_b$ and $\bar{x}$, and clearly, we have $\theta' \to 0$ when $\omega \to 0$ since the damping force is small in this case. Thus, the phase difference $\phi > 0$ is upper bounded by $\pi/2 + \theta'$ as $\omega$ reduces. Note that Eq. (60) defines an open interval for $T_d < 1$, and therefore $A_b$ must be sufficiently small if one aims to achieve vibration reduction when $\omega \to 0$ by conventional linear and HSLDS vibration isolators with positive stiffness $K > 0$ around the single equilibrium point $\bar{r} = 0$. However, it will significantly increase the isolator size given $A_b = \bar{A}_b/\bar{l}$.

As for the active BVI, $K < 0$ holds around $\bar{r} = 0$. Since the linear delayed feedback actuation (11) tuned as per Fig. 5 or Fig. 6 does not change the bistable characteristics and since a positive gain $D$ is beneficial as per Fig. 9-Fig. 13, the tuned feedback actuation $\bar{u}$ and the mechanical components $((\bar{k}_v, \bar{k}_h, \bar{k}_h), \bar{c})$ jointly function as a nonlinear negative-stiffness spring plus a positive damper. The forces applied on the proof mass of a BVI by the equivalent total stiffness and damping are denoted as $\bar{F}_e$ and $\bar{c}_e\bar{\omega}|\bar{r}|$, respectively. Note that $\bar{F}_e(|\bar{r}|) < 0$ around $\bar{r} = 0$, and the relationship between $\phi$ and such equivalent forces is demonstrated in Fig. 14(b), where the phase

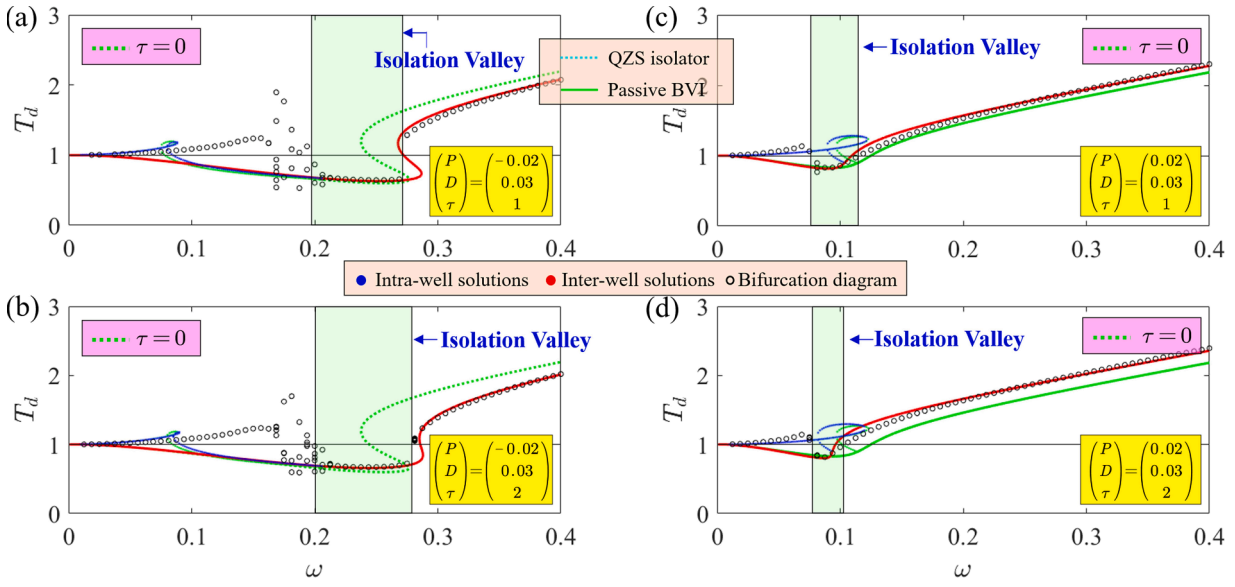


**Fig. 13.** Delay effects on the displacement transmissibility of the active BVI for ultra-low-frequency vibration isolation. The isolation valley is marked as the green bands. (a) and (b) are with $P < 0$ and $\tau = 1$. (c) and (d) are with $P > 0$ and $\tau = 2$.

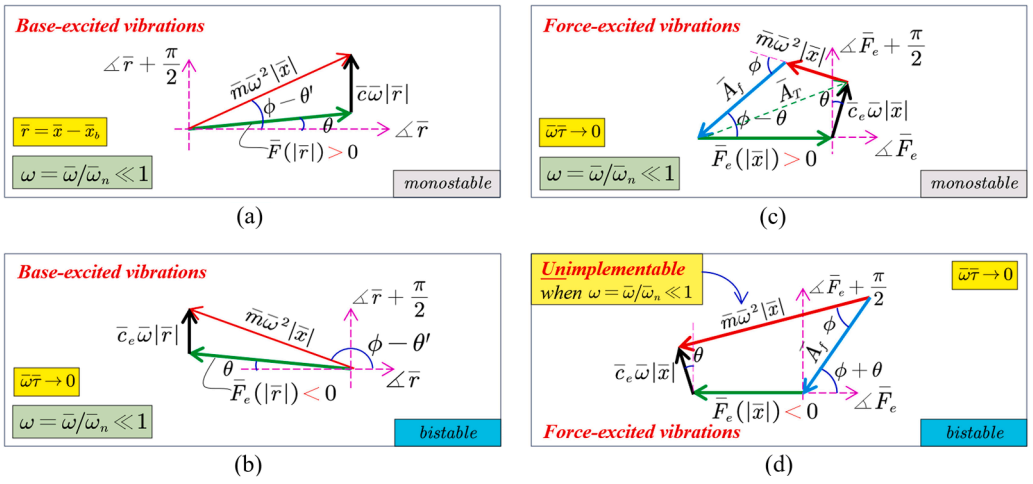


**Fig. 14.** Relationship between phase difference $\phi$ and forces exerted on the proof mass. (a-b). Base-motion-excited cases, in which (a) for monostable and (b) for bistable. (c-d). Force-excited cases, in which (c) for monostable and (d) for bistable.

difference $\omega\tau$ caused by delay is omitted, and the geometry condition $\phi \in (\pi/2, \pi)$ when $\theta \to 0$ corresponds to the isolation valleys as in Fig. 11, Fig. 12, and Fig. 13 for ultra-low-frequency vibration isolation. The correspondence between $\phi \in (\pi/2, \pi)$ and $K < 0$ signifies that the isolation valley with $T_d < 1$ when $\omega \to 0$ can be easily achieved by a BVI operating with inter-well motions. Fig. 14(c) and (d) are considered next.

### 5.3.4. *Discussions of ultra-low-frequency vibration isolation in force-excited cases*

Discussions on ultra-low-frequency vibration isolation have so far only focused on the base-motion-excited case. As for the force-excited case, combining Eqs. (34) and (54) yields

$$\ddot{x} + F_T = f, f = A_f \cos(\omega t + \phi). \tag{61}$$

The force transmissibility $T_f$ defined in (57) then has the equivalent form of

$$T_f = \frac{|F_T|}{|f|} = \frac{|f - \ddot{x}|}{|f|} = \frac{A_T}{A_f} = \frac{\sqrt{A_f^2 + (\omega^2 A_z)^2 + 2\omega^2 A_z A_f \cos(\phi)}}{A_f}, \tag{62}$$

which is similar to the expression of the displacement transmissibility $T_d$, see Eq. (59). Thus, the necessary condition $\phi \in (\pi/2, \pi)$ in (60) also applies to the force-excited case to achieve vibration reduction with $T_f < 1$. Note, however, that we have $\phi \in (0, \pi/2)$ for low-frequency excitations with $\omega \ll 1$ regardless of bistable and monostable vibration isolators since the excitation force $\bar{f} = A_f \cos(\omega t + \phi)$ is directly posed on the proof mas, exemplified by the constant-force case $\bar{\omega} = 0$ where $\mathrm{sgn}(\bar{x}) = \mathrm{sgn}(\bar{f})$. Consequently, isolating the ultra-low-frequency vibrations in the force-excited case to reduce the vibrations on the base is more challenging compared with the base motion-excited cases to settle the proof mass. Furthermore, we can conclude that the isolation valley with $T_f < 1$ as $\omega \to 0$ can hardly appear in the force-excited case.

More intuitively, we consider the relationship between the phase difference $\phi$ and the forces exerted on the proof mass. Following Fig. 14(b), we equate the feedback actuation $\bar{u}$ to a spring plus a positive damper and, accordingly, denote the forces produced by total equivalent stiffness and damping as $\bar{F}_e$ and $\bar{c}_e\bar{\omega}|\bar{x}|$, respectively. For conventional linear and HSLDS isolators, which are monostable systems with $\bar{F}_e(|\bar{x}|) > 0$ around $\bar{x} = 0$, the relationship between $\phi$ and forces on the proof mass is shown in Fig. 14(c), where the direction of the excitation vector signified by $\bar{A}_f = |\bar{f}|$ is reversed since $f$ is on the right side of Eq. (61). The dimensional amplitude of the forces exerted on the base as per Eq. (54) is marked as $\bar{A}_T$. When $\bar{\omega} \to 0$, we have $\phi \in (0, \pi/2)$, and hence, $\bar{A}_T > \bar{A}_f$ holds, leading to null vibration reduction $T_f > 1$.

As for the BVI, $\bar{F}_e(|\bar{x}|) < 0$, and the forces on the proof mass when the BVI is operating around $|\bar{x}| = 0$ to handle low-frequency force excitations with $\phi \in (0, \pi/2)$ are shown in Fig. 14(d). Notice that the geometric relationship reflected in Fig. 14(d) signifies that the two conditions $\bar{\omega} \to 0$ and $\phi + \theta \in (0, \pi/2)$ contradict each other, and thus no solutions exist around $|\bar{x}| = 0$ for a BVI when $\theta$ is negligible (i.e., $|d_2\bar{x}^2| \ll 1, |n_3\bar{x}^3| \ll |n_1\bar{x}|$). This observation indicates that large-amplitude motions tend to appear in the low-frequency band, consistent with Fig. 8(d-f). Since $\bar{F}_e(|\bar{x}|) > 0$ holds around the two stable equilibrium points $\bar{x}_1$ and $\bar{x}_2$, the large-amplitude motions crossing such two points lead to no vibration reduction $T_f > 1$ in light of Fig. 14(c). Consequently, the isolation valley is an exclusive strength of BVIs to isolate ultra-low-frequency base-motion-excited vibrations through inter-well motions, which is an important guideline for the practical BVI design.

## 6. Conclusions

We drive a classic BVI construction with a PD-type feedback actuation aiming for performance enhancement. Particularly, we additionally inject a bias term and a delay into the control logic to manipulate intra- and inter-well operating modes and to evaluate the effect of control parameters and the inevitable loop delay on system stability, bistable dynamics, and vibration isolation. Important results and design rules arising from this work are as follows.

- Feedback actuation should not change the instability of the saddle equilibrium $x_0$ and the stability of the remaining two $x_1$ and $x_2$. Besides, the loop delay can be treated as an effective tunable control parameter for performance enhancement. The gain intervals of $(P, D)$ where the active BVI is operable independent of delay are obtained to enhance the control robustness against delay perturbations.
- For delay-coupled bistable dynamics analysis, taking the isolator as phase zero reduces the number of variables, and sweeping the frequency when solving equations eliminates transcendentality. The resulting time costs of calculations based on Padé approximation and the resultant concept following [46] can be reduced by more than 90 % in comparison. The much-reduced computational costs indicate that the Padé approximation, which outperforms the widely adopted Tylor's series, can be an alternative to handle nonlinear dynamics of large deflections or amplitudes for higher accuracy.
- Vibration isolation performance of a BVI is related to frequency responses. For intra-well motions, the BVI exhibits HSLDS characteristics yielding broadband vibration isolation, and the feedback actuation tuned with a negative gain $P$ and a positive gain $D$ further extends the isolation band and reduces the peak transmissibility amplitude. In addition, the often-overlooked loop delay provides a beneficial damping effect.
- For inter-well motions, feedback actuation can relax the issues of passive BVIs that the width of the exclusive isolation valley for ultra-low-frequency vibration isolation is too narrow to be practically utilized. Increasing and decreasing the gain $P$ shifts the valley leftward and rightward, respectively, and increasing the gain $D$ suppresses aperiodic dynamics and broadens valley width. Hence, the isolation valley can be considerably extended and freely manipulated by tuning the gain pair $(P, D)$ in real-time. On the other hand, increasing the loop delay extends and narrows the valley for a negative and positive gain $P$, respectively, a guidance for the feedback loop design.
- Compared to conventional HSLDS vibration isolators, the BVI, which can operate with intra- and inter-well motions, presents an additional operating mode. A properly designed control logic helps users switch or select between such two modes to activate broadband or ultra-low-frequency vibration isolation. In particular, the ultra-low-frequency vibration isolation by achieving isolation valley is an exclusive strength of the BVI to isolate base vibrations.

Finally, the given control stability analysis, simplified dynamical analysis, tuning rules of delayed feedback actuation, as well as the revealed benefits of the active BVI over the passive ones and the HSLDS isolators altogether complement and extend the theories developed in our previous works [37,46]. With the established design rules and analysis tools, our future work includes achieving ultra-low-frequency vibration isolation and energy harvesting simultaneously to design a self-powered active BVI. Different from the present BVI resulting from geometry nonlinearity, a BVI with material nonlinearity or other nonlinear mechanisms will be investigated to simplify mechanical design and enhance structural robustness for real applications.

### CRediT authorship contribution statement

**Yifan Liu:** Conceptualization, Investigation, Writing – original draft, Writing – review & editing. **Bo Yan:** Conceptualization, Funding acquisition, Writing – review & editing. **Li Cheng:** Project administration, Supervision, Writing – review & editing.

### Declaration of Competing Interest

The authors declare that they have no known competing financial interests or personal relationships that could have appeared to influence the work reported in this paper.

### Data availability

Data will be made available on request.

### Acknowledgments

This work is partially supported by the National Natural Science Foundation of China (Grant No. 52175125).

### References

[1] C.E. Crede, Vibration and Shock Isolation, Wiley, 1951.
[2] C.W. De Silva, Vibration and Shock Handbook, CRC press, 2005.

[3] J.C. Snowdon, Vibration isolation: use and characterization, J. Acoust. Soc. Am. 66 (1979) 1245–1274.
[4] J.P. Den Hartog, Mechanical Vibrations, Courier Corporation, 1985.
[5] B. Yan, N. Yu, C. Wu, A state-of-the-art review on low-frequency nonlinear vibration isolation with electromagnetic mechanisms, Appl. Math. Mech. 43 (2022) 1045–1062.
[6] A. Carrella, M. Brennan, T. Waters, Static analysis of a passive vibration isolator with quasi-zero-stiffness characteristic, J. Sound. Vib 301 (2007) 678–689.
[7] A. Carrella, M. Brennan, T. Waters, K. Shin, On the design of a high-static–low-dynamic stiffness isolator using linear mechanical springs and magnets, J. Sound. Vib 315 (2008) 712–720.
[8] B. Tang, M. Brennan, On the shock performance of a nonlinear vibration isolator with high-static-low-dynamic-stiffness, Int. J. Mech. Sci. 81 (2014) 207–214.
[9] R. Ibrahim, Recent advances in nonlinear passive vibration isolators, J. Sound. Vib 314 (2008) 371–452.
[10] I. Kovacic, M.J. Brennan, T.P. Waters, A study of a nonlinear vibration isolator with a quasi-zero stiffness characteristic, J. Sound. Vib 315 (2008) 700–711.
[11] A. Carrella, M. Brennan, I. Kovacic, T. Waters, On the force transmissibility of a vibration isolator with quasi-zero-stiffness, J. Sound. Vib 322 (2009) 707–717.
[12] A. Carrella, M. Brennan, T. Waters, V. Lopes Jr, Force and displacement transmissibility of a nonlinear isolator with high-static-low-dynamic-stiffness, Int. J. Mech. Sci. 55 (2012) 22–29.
[13] M. Brennan, I. Kovacic, A. Carrella, T. Waters, On the jump-up and jump-down frequencies of the Duffing oscillator, J. Sound. Vib 318 (2008) 1250–1261.
[14] D. Xu, Q. Yu, J. Zhou, S. Bishop, Theoretical and experimental analyses of a nonlinear magnetic vibration isolator with quasi-zero-stiffness characteristic, J. Sound. Vib 332 (2013) 3377–3389.
[15] J. Zhou, X. Wang, D. Xu, S. Bishop, Nonlinear dynamic characteristics of a quasi-zero stiffness vibration isolator with cam–roller–spring mechanisms, J. Sound. Vib 346 (2015) 53–69.
[16] K. Ye, J. Ji, T. Brown, A novel integrated quasi-zero stiffness vibration isolator for coupled translational and rotational vibrations, Mech. Syst. Signal. Process 149 (2021), 107340.
[17] J. Bian, X. Jing, Analysis and design of a novel and compact X-structured vibration isolation mount (X-Mount) with wider quasi-zero-stiffness range, Nonlinear. Dyn 101 (2020) 2195–2222.
[18] Y. Chai, X. Jing, X. Chao, X-shaped mechanism based enhanced tunable QZS property for passive vibration isolation, Int. J. Mech. Sci. 218 (2022), 107077.
[19] X. Chong, Z. Wu, F. Li, Vibration isolation properties of the nonlinear X-combined structure with a high-static and low-dynamic stiffness: theory and experiment, Mech. Syst. Signal Process 179 (2022), 109352.
[20] G. Yan, Z.-Y. Wu, X.-S. Wei, S. Wang, H.-X. Zou, L.-C. Zhao, W.-H. Qi, W.-M. Zhang, Nonlinear compensation method for quasi-zero stiffness vibration isolation, J. Sound Vib 523 (2022), 116743.
[21] X. Wang, H. Liu, Y. Chen, P. Gao, Beneficial stiffness design of a high-static-low-dynamic-stiffness vibration isolator based on static and dynamic analysis, Int. J. Mech. Sci. 142 (2018) 235–244.
[22] X. Sun, J. Xu, X. Jing, L. Cheng, Beneficial performance of a quasi-zero-stiffness vibration isolator with time-delayed active control, Int. J. Mech. Sci. 82 (2014) 32–40.
[23] X. Sun, J. Xu, J. Fu, The effect and design of time delay in feedback control for a nonlinear isolation system, Mech. Syst. Signal Process 87 (2017) 206–217.
[24] T. Yang, Q. Cao, Noise-and delay-enhanced stability in a nonlinear isolation system, Int. J. Non. Linear. Mech 110 (2019) 81–93.
[25] C. Cheng, Y. Hu, R. Ma, W. Wang, Beneficial performance of a quasi-zero-stiffness vibration isolator with displacement-velocity feedback control, Nonlinear. Dyn 111 (2023) 5165–5177.
[26] B. Yan, X. Wang, H. Ma, W. Lu, Q. Li, Hybrid time-delayed feedforward and feedback control of lever-type quasi-zero-stiffness vibration isolators, IEEE. Transac. Ind. Elect. 71 (2024) 2810–2819.
[27] N. Yu, H. Ma, C. Wu, G. Yu, B. Yan, Modeling and experimental investigation of a novel bistable two-degree-of-freedom electromagnetic energy harvester, Mech. Syst. Signal Process 156 (2021), 107608.
[28] X. Li, D. Yurchenko, R. Li, X. Feng, B. Yan, K. Yang, Performance and dynamics of a novel bistable vibration energy harvester with appended nonlinear elastic boundary, Mech. Syst. Signal Process 185 (2023), 109787.
[29] S. Fang, S. Zhou, D. Yurchenko, T. Yang, W.-H. Liao, Multistability phenomenon in signal processing, energy harvesting, composite structures, and metamaterials: a review, Mech. Syst. Signal Process 166 (2022), 108419.
[30] D.R. Johnson, M. Thota, F. Semperlotti, K. Wang, On achieving high and adaptable damping via a bistable oscillator, Smart Mater. Struc. 22 (2013), 115027.
[31] Z. Lu, T. Yang, M.J. Brennan, Z. Liu, L.-Q. Chen, Experimental investigation of a two-stage nonlinear vibration isolation system with high-static-low-dynamic stiffness, J. Appl. Mech 84 (2017), 021001.
[32] S. Ishida, H. Uchida, H. Shimosaka, I. Hagiwara, Design and numerical analysis of vibration isolators with quasi-zero-stiffness characteristics using bistable foldable structures, J. Vib. Acoust (2017) 139.
[33] K. Yang, W. Tong, L. Lin, D. Yurchenko, J. Wang, Active vibration isolation performance of the bistable nonlinear electromagnetic actuator with the elastic boundary, J. Sound. Vib 520 (2022), 116588.
[34] K. Yang, R. Harne, K. Wang, H. Huang, Investigation of a bistable dual-stage vibration isolator under harmonic excitation, Smart Mater. Struc. 23 (2014), 045033.
[35] B. Yan, H. Ma, B. Jian, K. Wang, C. Wu, Nonlinear dynamics analysis of a bi-state nonlinear vibration isolator with symmetric permanent magnets, Nonlinear Dyn 97 (2019) 2499–2519.
[36] B. Yan, H. Ma, L. Zhang, W. Zheng, K. Wang, C. Wu, A bistable vibration isolator with nonlinear electromagnetic shunt damping, Mech. Syst. Signal. Process 136 (2020), 106504.
[37] B. Yan, N. Yu, H. Ma, C. Wu, A theory for bistable vibration isolators, Mech. Syst. Signal. Process 167 (2022), 108507.
[38] J. Noh, P. Kim, Y.-J. Yoon, Competitive advantages of a bistable vibration isolator: cut-off frequency and operational safety near harmful resonance, J. Sound. Vib 570 (2024), 118004.
[39] J. Cai, Y. Liu, Q. Gao, Y. Chen, Spectrum-based stability analysis for fractional-order delayed resonator with order scheduling, J. Sound. Vib 546 (2023), 117440.
[40] Z. Šika, J. Krivošej, T. Vyhlídal, Three dimensional delayed resonator of Stewart platform type for entire absorption of fully spatial vibration, J. Sound. Vib (2023), 118154.
[41] A. Saldanha, W. Michiels, M. Kuře, J. Bušek, T. Vyhlídal, Stability optimization of time-delay systems with zero-location constraints applied to non-collocated vibration suppression, Mech. Syst. Signal. Process 208 (2024), 110886.
[42] J. Cai, Q. Gao, Y. Liu, N. Olgac, Control design, analysis, and optimization of fractional-order delayed resonator for complete vibration absorption, J. Sound. Vib 571 (2024), 118083.
[43] H. Silm, M. Kuře, J. Bušek, W. Michiels, T. Vyhlídal, Spectral design and experimental validation of noncollocated vibration suppression by a delayed resonator and time-delay controller, IEEE. Transac. Control Syst. Technol. (2023).
[44] Y. Liu, J. Cai, N. Olgac, Q. Gao, A robust delayed resonator construction using amplifying mechanism, J. Vib. Acoust 145 (2023), 011010.
[45] D. Huang, S. Zhou, R. Li, D. Yurchenko, On the analysis of the tristable vibration isolation system with delayed feedback control under parametric excitation, Mech. Syst. Signal. Process 164 (2022), 108207.
[46] Y. Liu, J. Cai, L. Hou, B. Yan, L. Chen, Q. Gao, Bistable dynamics analysis using Padé approximation and resultant theory, Int. J. Non. Linear Mech 149 (2023), 104325.
[47] V.B. Kolmanovskii, V.R. Nosov, Stability of Functional Differential Equations, Elsevier, 1986.
[48] A. Ukil, V.H. Shah, B. Deck, Fast computation of arctangent functions for embedded applications: a comparative analysis, in: 2011 IEEE International Symposium on Industrial Electronics, IEEE, 2011, pp. 1206–1211.
[49] T. Vyhlidal, P. Zítek, Mapping based algorithm for large-scale computation of quasi-polynomial zeros, IEEE. Trans. Automat. Contr 54 (2009) 171–177.

[50] P.M. Nia, R. Sipahi, Controller design for delay-independent stability of linear time-invariant vibration systems with multiple delays, J. Sound Vib 332 (2013) 3589–3604.
[51] C.M. Bender, S.A. Orszag, Advanced Mathematical Methods For Scientists and Engineers I: Asymptotic methods and Perturbation Theory, Springer Science & Business Media, 1999.
[52] G. Gatti, Statics and dynamics of a nonlinear oscillator with quasi-zero stiffness behaviour for large deflections, Commun. Nonlinear. Sci. Numer. Simul. 83 (2020), 105143.
[53] S.C. Stanton, B.A. Owens, B.P. Mann, Harmonic balance analysis of the bistable piezoelectric inertial generator, J. Sound. Vib 331 (2012) 3617–3627.
[54] A. Edelman, H. Murakami, Polynomial roots from companion matrix eigenvalues, Math. Comput 64 (1995) 763–776.
[55] G.E. Collins, The calculation of multivariate polynomial resultants, JACM 18 (1971) 515–532.
[56] J.J. Sylvester XXIII, A method of determining by mere inspection the derivatives from two equations of any degree, London,. Edinburgh,. Dublin. Phil. Magazine. and. Journal. of. Science 16 (1840) 132–135.
[57] G. Liu, J.-k. Liu, L. Wang, Z.-r. Lu, A new semi-analytical approach for quasi-periodic vibrations of nonlinear systems, Commun. Nonlinear. Sci. Numer. Simul. 103 (2021), 105999.